UNIVERSIDAD DE SANTIAGO DE CHILE

FACULTAD DE CIENCIA

DEPARTAMENTO DE FÍSICA

Design and properties of Bimetallic Nanostructures: Structural and mechanical properties of stable systems

Javier Esteban Rojas Núñez

Profesores Guía:

Samuel Baltazar Rojas

Dora Altbir Drullinsky

Tesis para optar al grado de Doctor
en Ciencia con Mención en Física

Santiago – Chile
2019

Design and properties of Bimetallic Nanostructures:
Structural and mechanical properties of stable systems

Javier Esteban Rojas Núñez

Este trabajo de titulación fue preparado bajo la supervisión de los profesores guía Dr. Samuel Baltazar Rojas y Dra. Dora Altbir Drullinsky del Departamento de Física y ha sido aprobado por los siguientes miembros de la comisión calificadora del candidato:

Dr. Samuel Baltazar Rojas

Dra. Dora Altbir Drullinsky

Dr. Francisco Muñoz Saez

Dra. Paola Arias Reyes

Dr. Sebastián Allende Prieto

Dr. Nicolás Arancibia Miranda

Dr. Guillermo Romero Huenchuñir
DIRECTOR PROGRAMA
DE DOCTORADO
FACULTAD DE CIENCIA

Sr. Roberto Bernal Valenzuela
DIRECTOR DEL DEPARTAMENTO
DE FÍSICA
FACULTAD DE CIENCIA

Abstract

The study of bimetallic nanoparticles has grown in the last years, from a theoretical and experimental perspective, due to the numerous applications envisaged in areas such as electronics, catalysis, and environmental issues, among others. Even thought, the large number of possible configurations for bimetallic nanoparticles left a broad spectrum of structures unexplored yet, in part because of the synthesis difficulties or due to complex atomic arrangements as the size becomes large.

In this thesis, a theoretical modeling technique is proposed to scale the usability of several optimization methods at nanometric sizes. This technique is based on a smart selection of initial configurations, combined with local optimization methods to enclose the search into reasonable motifs. The obtained results are comparable to experimentally synthesized nanoparticles.

With this methodology, bimetallic systems such as FeCu, AgCu, and FeNi were studied, establishing a relationship between morphology and element concentration. In particular, we have obtained specific conditions to get core-shell and Janus motifs, along with other metastable configurations. Such results were compared with experimental synthesis, achieving an excellent agreement with them.

The application of this procedure is not restricted only to metallic nanoparticles but could be applied to other nanostructures, based on segregated compounds. An example of these applications is the case for bimetallic nanotubes, with a mechanical performance modulated respect to the monoatomic cases. The study of these systems envisaged an excellent projection of these kinds of methodologies to study material properties at the nanoscale level, which can lead to the creation of intelligent designs for nanostructures.

Keywords: nanoparticles, nanowires, bimetallic, neural networks, nanotechnology.

Dedicado a mis padres y hermanos. Ellos, quienes han sido el bastión donde pude cobijarme en los tiempos adversos. Este trabajo ha marcado el inicio de una nueva etapa, de la cual, quiero que se sepan partícipes. Por esto y mucho más, se los dedico con mi más profunda gratitud.

Acknowledgements

From a personal perspective I want to acknowledge to my family, in particular to my parents and brothers, whose inconditional love and support helped me along my years as a student.

From a professional point of view, this work was possible thanks to the support of several people from various institutions. In first place, I want to acknowledge my advisors Dr. Samuel Baltazar Rojas and Dra. Dora Altbir Drullinsky for the wisdom provided along my studies. Thanks to my collaborators from *Universidad de Santiago de Chile, Universidad de Mendoza, Universidad Austral de Chile, Universidad Mayor*, PennState University, and Binghamton University for their work involved in publications along this thesis.

Also thanks to the evaluation committee, constituted by Dr. Francisco Muñoz Saez, Dra. Paola Arias Reyes, Dr. Sebastián Allende Prieto and Dr. Nicolás Arancibia Miranda, for their time and feedback provided into the review of this work.

And finally thanks to the financial support provided by CEDENNA, DICYT and CONICYT. CONICYT in particular, provided the funding to my PhD throught its scholarship "Beca doctorado Nacional" PCHA-21150699.

Contents

List of Tables

List of Figures

Introduction

Nanostructures are, by definition, atomic arrangements with at least one or more dimensions in the nanometer scale (≤ 100 nm).[1] In these range of sizes, the structures have an important surface–volume ratio, and therefore, the nanoparticle surface plays a more significant role in their properties compared to bulk systems.

In nanoparticles, surface effects modify the properties of the system, differentiating them from their bulk counterparts, such as melting point.[2] The size of these structures becomes important due to quantum effects that are present in small finite systems [3, 4], leading in particular to changes in the optical properties, such as the shift of the plasmon resonance of metallic systems. These size effects have been already reported for several systems such as Pt and Au particles, finding the quantum behavior and the plasmon redshifted wavelength as the nanoparticle size is increased, respectively.[5, 6]

Additionally to the size, shape is also an essential characteristic for nanoparticles. Metallic nanoparticles have been synthesized into different patterns such as cubical, octahedral, hexagonal and icosahedral shapes, among others.[7] These shapes are built by exposing particular crystal planes, leading to changes in plasmonic resonance [8, 9, 10] and catalysis performance.[11]

A new degree of freedom can be added to nanostructures properties when another metallic element gets into the mix, leading to bimetallic systems. In bimetallic nanoparticles, these two metallic elements are present in several elemental concentrations and can be arranged in different distributions. The work of Ferrando et al.[12] classifies these distributions in four categories: Core-shell, subcluster segregated (also known as Janus structures), mixed nanoalloys and multishell nanoalloys. The concentration and size of bimetallic configurations are characteristics considered at experimental level to modulate the properties of the material, changing its morphology and corresponding properties.[13, 14, 15, 16, 17, 18, 15] In this context, we expect that the properties of bimetallic nanostructurated systems can also be affected by the elemental distribution of their atoms.[19]

All these characteristics give versatility to mono/bi–metallic systems properties. This versatility makes structures, such as nanoparticles or nanowires, ideal candidates for a wide number of applications in medicine, catalysis, and water remediation among others.[20, 21, 16, 22] In the particular case of bimetallic nanoparticles, the "*synergistic effect*" and their additional degree of freedom makes them more appealing.[23]

The advantages of nanoparticles can be extended to other nanostructures, which do not have all their dimensions restricted to the nanoscale, such as nanowires.[24, 25, 26, 27, 28] These nanostructures can also get their properties optimized by changing the structure[26] or the elemental concentration.[24, 25]

All these structures are present in a variety of sizes, which is a key factor to modulate their properties.[15, 21, 29] As a consequence, the number of configurations grows exponentially with the size of the system, leading to an unknown amount of configurations yet to be found at different sizes.[30] To explore all these configurations, theoretical approaches are used to calculate the energy of atomic arrangements to produce an energy landscape, also known as potential energy surface (PES). The PES can be then explored using numerical algorithms to model the atomic arrangements into configurations that are in the local minima of the energy landscape. This process will be referenced as theoretical modeling and it allows to get stable configurations, only limited by the capabilities of the considered computational algorithms.

Besides this, nanostructures such as one-dimensional metallic and magnetic nanostructures have attracted significant attention in the last decades. The former is due to their applications in nanodevices with high mechanical strength and conductivity,[31, 32, 33] as well as their optical and electronic properties owing to their confinement effects.[34] One of the aspects to consider in one dimensional systems, such as nanowires, is the metal concentration on bimetallic structures. The bimetallic nanowires have great importance not only because of the properties of both metals, but also due to the usually improved electronic, magnetic, and optical properties.[33] In particular, these nanowires could present ballistic conductivity and can be potentially used as components of nanoelectronic devices.[35] Based on this evidence, it is expected that the modulation of material and geometric parameters, could lead to improved mechanical response of bimetallic grain-based nanowires and nanotubes.

State of the art

The current status in theoretical modeling is centered on solving the global optimization problem for the energy of atomistic systems. This has been discussed in detail in a review reported by Francesca Baletto [36]. All methods presented in this review are applied to structures under 1000 atoms, which is not enough to reach the larger synthesized system sizes of 5 nm diameter and above, that are used to tune properties in the previously mentioned applications. The system energy calculations used in these global optimization studies can be classified in ab-initio approaches and classical potentials, as they are stated in Baletto's review.[36] The ab-initio approaches, such as density functional theory, are one of the most accurate methods to calculate the system energy, but they demand a great amount of computational resources. This topic will be discussed in more detail in chapter 1. There is also some development in the use of machine learning to get density functional theory accuracy level of energies and forces with a noticeable reduce in computational cost [37, 38], which makes them an interesting approach in the future. In the state of the art, nanostructures are theoretically modeled only for small nanostructure sizes.[36] Nevertheless, another approach is necessary as the system grows to reduce the exploration zone while it keeps its effectiveness to get the lowest energy structure possible.

Hypothesis and goals

In bimetallic nanostructures, the combination of two elements can change the system morphology and properties. This effect, combined with size and morphology, is expected to modulate structural and mechanical properties. To accomplish this work will achieve the following goals:

General: To study stable bimetallic nanostructurated systems.

Specific goals:

- To understand the theoretical tools developed to explore the configuration landscape or potential energy surface (PES).
- To implement a modified method to explore the PES of nanometric size systems.
- To get a correlation between size, concentration, and morphologies for nanostructures.
- To study nanostructure properties for bimetallic systems.

Overview

In this work the properties of bimetallic nanostructures will be studied. Bimetallic nanoparticles and nanowires will be covered in this work. The whole thesis will be divided in three chapters.

In the first chapter, different searching methods and energy calculations are explored, looking for convenient approaches to use at nanometric size scales.

Then, in the second chapter, a searching method is proposed to look for stable bimetallic nanoestructure for large atomic systems. FeCu, CuAg, and FeNi bimetallic systems are selected to use this methodology with different metallic elements. Also in this chapter, a neural network based potential is tested against conventional classical potentials showing the margin of improvement using these novel potentials.

In the third chapter, mechanical properties of one dimensional systems are studied. In a first stage, Ni nanowires and nanotubes are compared looking for differences under compressive and tensile deformations. The second stage covers the difference between a bimetallic FeNi nanowire and its separated counterparts, also under tensile and compressive deformations.

Finally, general conclusions about this work and their implications are summarized.

Chapter 1

Theoretical background

1.1 Introduction

The modeling of nanoparticles strongly contributes to the understanding of their properties. This process requires to know how atoms will be arranged when each nanostructure is synthesized. For this purpose, atomistic calculations have to be done to find the most suitable atomic arrangement. These calculations require two key components: an energy calculation method and a searching method to explore different configurations in the energy landscape.

1.2 Energy calculations

Energy calculations are a fundamental part of atomistic simulations because they are the bridge between simulations and reality. One of the most relevant aspects of energy calculations is that they form an object called the potential energy surface (PES). In the PES, the energies and their gradients (forces) are asociated to every atomistic configuration of the system. The energy and force are used to find local energy minima configurations of a system, being the lowest of them called the ground state.

The ground state is crucial because every system tends to minimize its energy, i.e., any structure tends to go to this state. Because of this tendency, it is reasonable to look for the ground state and assume it as a stable configuration.

There are two different approaches to calculate this interaction potential: an ab-initio approach and a phenomenological approach. Ab-initio approaches consider the electrons and ions of the atomic system, and phenomenological ones correspond to a classical approach, which models atomic interactions. These approaches will be presented here by using density functional theory, embedded atom method-like potentials, and neural networks.

1.2.1 Density functional theory

The density functional theory (DFT) takes the ab-initio approach, and this implies that the energy of the system is calculated using the fundamental hamiltonian of the system (H), which includes electron interactions. In this approach, the energy of the system (E) is obtained by solving the many-body Schrödinger's equation, that is,

$$H\left|\psi\right\rangle = E\left|\psi\right\rangle . \tag{1.1}$$

To address this problem the variational principle can be used, which says that every trial wave function used to solve the Schrödinger's equation will give an energy higher than the one obtained using the ground state wave function. This technique is the basic principle that was used in the Hartree-Fock method to solve these systems.[39]

The Hartree-Fock method takes multiple resources to get the solution for systems with many electrons, because of the increasing number of variables. Then this problem was reduced assuming that the energy could be written as a function of the electronic density of the system ρ

$$\begin{aligned} E &= E\left[\rho\right], \\ \rho\left(\vec{r}\right) &= \int\cdots\int\left|\psi\left(\vec{r},\vec{r_1},\cdots,\vec{r_N}\right)\right|^2 d\vec{r}d\vec{r_1}\cdots d\vec{r_N}. \end{aligned} \tag{1.2}$$

This idea got its theoretical origin in 1964 when Hohenberg and Kohn showed that $E[\rho]$ was minimized when the ground state electronic density was used [40]. Even though this functional relation was useful, the functional itself was not specified. Therefore, all that is needed is the exact functional $E[\rho]$. The energy functional is written as

$$E[\rho] = T_s[\rho] + E_H[\rho] + E_{ext}[\rho] + E_{XC}[\rho]. \tag{1.3}$$

In this functional, all the terms are precisely known, except the exchange and correlation functional ($E_{XC}[\rho]$), which includes the correction for interaction and correlation of kinetic ($T_S[\rho]$) and Hartree ($E_H[\rho]$) energy functionals. This exchange and correlation functionals are relatively small, so it is possible to express them as a local approximation:

$$E_{XC}[\rho] = \int d^3\vec{r}\rho\left(\vec{r}\right)\varepsilon_{XC}\left(\rho,\vec{\nabla}\rho\right), \tag{1.4}$$

where ε_{XC} is the exchange-correlation energy density per electron. This exchange and correlation functional can also depends on the spin polarization of the electron density, which is expressed as a fractional polarization term

$$\zeta = \frac{\rho_\uparrow - \rho_\downarrow}{\rho_\uparrow + \rho_\downarrow} = \frac{\rho_\uparrow - \rho_\downarrow}{\rho} \tag{1.5}$$

Here $\rho_\uparrow$ ($\rho_\downarrow$) represents the polarized electronic density with up (down) spin. This variable allows a better description of real systems that present spin polarization, such as magnetic systems. Considering this degree of freedom, a more general expression for E_{XC} is obtained as

$$E_{XC} = E_X + E_C = \int d^3\vec{r}\rho\left(\vec{r}\right)\left(\varepsilon_X + \varepsilon_C\right) = \int d^3\vec{r}f\left(\rho,\zeta,\nabla\rho\right). \tag{1.6}$$

This expression can be defined by different approximations, such as local spin density approximation (LSD), generalized gradient approximation (GGA) and hybrid functional methods. These approximations consider density dependence, density and density gradient dependence, and a mixture of different approaches respectively. In this work, the GGA method will be used, more specifically, the one developed by Perdew, Burke, and Ernzerhof, also known as the PBE parameterization.[41, 42]

In PBE's work [41, 42] an analytical parameterization was proposed considering the Lieb-Oxford bound, a uniform density scaling and a linear response. The form of this functional involves a correction function (F_{XC}) over the homogeneous electron exchange ε_X^{HOM},

$$E_{XC} = \int d^3\vec{r}\rho\left(\vec{r}\right)\varepsilon_X^{HOM}(\rho)F_{XC}(\rho,\zeta,\nabla\rho). \tag{1.7}$$

Here the correlation functional is considered inside the correction function.

As is stated in the PBE's work [41, 42], this approach left behind some minor features to keep it in a simple form. These features are, "*correct second-order gradient coefficients for E_x and E_c in the slowly varying limit*" and "*correct non-uniform scaling of E_x in limits where the reduced gradient s*[1] *tends to infinity*". Even though, these compromises were a fair trade to "*obtain fair accuracy for systems ranging from molecules to solids*" [43].

The main drawback for an ab-initio approach is computational cost, which makes it impossible to compute energies for large systems in reasonable time periods.

1.2.2 Interatomic potentials and embedded atom model

Interatomic potentials use the phenomenological approach that models interactions between atoms, i.e., bonds. This simplification implies that interatomic potentials do not compute an electronic configuration as ab-initio calculations do. Interatomic potentials

---

[1] This reduced gradient "s" in original work is proportional to the ratio between density gradient and density.

are less time consuming than ab-initio calculations but at the same time they are less accurate and precise. The basic behavior of interatomic potentials is based on short-range and long-range interactions between atoms. Among the short-range interactions, repulsive behavior will be present because of Coulomb repulsion between ions and Pauli's exclusion law. On the long-range interaction side, there is an attraction due to the dispersion energy better explained by the Drude model [44]. The most straightforward interaction scheme that handles these push/pull forces are pair interaction potentials. An example of pair interaction potential is the Lennard-Jones model, which was intended to model closed shell atomic systems with decent accuracy.

For metallic systems exist interatomic potential inspired in the local density approximation of DFT, which is the unpolarized spin version of LSD. This interaction scheme is the embedded-atom model (EAM), and it has two terms:

$$E_i = F_i\left(\sum_{j\neq i}\rho_j(r_{ij})\right) + \frac{1}{2}\sum_{j\neq i}\phi_{ij}(r_{ij}). \tag{1.8}$$

The first term is called an embedded function (F_i). The embedded function is a non-linear term that models the interaction between an atom with the surrounding homogeneous electronic cloud in the system (excluding its own electrons). The second term is the pair-interaction between atoms. There is no restriction about how the functions $\rho_j(r_{ij})$, $\phi_{ij}(r_{ij})$ and $F_i(\rho_j)$ have to be, except for the non-linearity in $F_i(\rho_j)$. This nonlinearity makes EAM potentials an effective many-body interaction.

The many-body nature of EAM makes this potential agreeably describes grain-boundary, dislocation, and surface energies on metallic systems when it is compared to experimental data [45]. This agreement is highly dependent on the parametrization of the potential and the theory which backs it up. On the other side, the spherical symmetry of EAM comes with the unavailability to represent angular bonds like most covalent bonding.

1.2.3 Artificial neural networks and interpolation of DFT

There is another alternative to the previously mentioned interaction potentials: artificial neural networks (ANN). These ANN's are machine learning algorithms, which according to Mitchel should: "(...) *learn from experience E with respect to some class of tasks T and performance measure P, if its performance at tasks in T, measured by P, improves with experience E*" [46]. Machine learning algorithms, such as ANN techniques, make it possible to handle extremely difficult to program tasks by simply teaching them instead of programming them directly. Some examples of these are: classification tasks [47], transcription [48], translation [49, 50], among others.

It is important to know first how ANN are built and trained, so we start with the basic structure of them. In ANNs exist simple functions called neurons or nodes, which takes some input values (x_i) and gives an output result (f_n). These nodes are often based on nonlinear functions (phi), such as $tanh(x)$, and a series of weights (w_n) and biases (b_n):

$$f_n = \sum_i \phi(w_n x_i + b_n). \tag{1.9}$$

To make use of these neurons, they are arranged in ordered layers ($f^{(m-1)}$) that are inputs from the previous layer ($f^{(m-2)}$) and provide a collection of outputs to the next layer ($f^{(m)}$). This kind of neural networks are called feedforward neural networks, also known as multilayer perceptrons. A generic mathematical representation can be written as

$$f(\vec{X}) = f^{(m)}\left(f^{(m-1)}\left(\cdots\left(f^{(1)}(\vec{X})\right)\right)\right). \tag{1.10}$$

The last layer ($f^{(m)}$) of a feedforward neural network is called the output layer, and it is the one needed to compare with the training set, or experience (E), to generate a performance measure (P). The main practical restriction for this ANN is the necessity of a fixed number of inputs ($\vec{X}$).

Now that the neural network structure is clear, it is time to train the algorithm. To do this, and as it has been told before, a machine learning algorithm must be capable of learning from experience. The training process requires a cost function (J), which determines how similar are the results of the neural network and the training set. This cost function must reach its minimum value when the performance of the algorithm is the best, i.e., it is the best fit with respect to the training set. This way the network is trained by using a minimization routine over the cost function, such as conjugate gradient.

Finally, with all the previous details addressed, it is time to apply a neural network to predict energies based on atom positions. This neural network will be called neural network potential (NNP) from now on. There are certain restrictions that inputs must meet to make this NNP work, such as been independent of the system size, and invariant to rotations and translations. Behler and Parrinello proposed a solution to these problems in 2007 using local symmetry descriptors [37]. There are two families of descriptors: one based in radial symmetry functions (G_i^1), and the other one in angular terms (G_i^2):

$$G_i^1 = \sum_{j\neq i} e^{-\eta(R_{ij}-R_S)^2} f_c\left(R_{ij}\right) \tag{1.11}$$

$$\begin{aligned} G_i^2 = 2^{1-\zeta} &\sum_{j\neq i} \left(1+\lambda\cos\left(\Theta_{ijk}\right)\right)^{\zeta} e^{-\eta\left(R_{ij}^2+R_{ik}^2+R_{jk}^2\right)} \\ &* f_c\left(R_{ij}\right) f_c\left(R_{ik}\right) f_c\left(R_{jk}\right) \end{aligned} \tag{1.12}$$

These descriptors have fixed parameters $\lambda = \pm 1$, η, and ζ, which are not unique and must be chosen to describe the atom local environment as good as possible. There is also the common used interatomic distances ($R_{ij} = \left|\vec{R_{ij}}\right| = |r_i - r_j|$), angles ($\Theta_{ijk} = \frac{\vec{R_{ij}}\cdot\vec{R_{ik}}}{R_{ij}R_{ik}}$), and cutoff functions:

$$f_c(x) = \begin{cases} 0.5 * \left[\cos\left(\frac{nR_{ij}}{R_c}\right)+1\right] & \text{for } R_{ij} \leq R_c, \\ 0 & \text{for } R_{ij} > R_c, \end{cases} \tag{1.13}$$

with R_c their cutoff radius. Even though these descriptors use the same local description as many interatomic potentials, the neural network treatment gives greater flexibility to the energy interpolation of the model, gaining accuracy compared to normal interatomic potentials.

To train these potentials exists a hierarchical way proposed by Hajinazar et al.,[51] which trains multicomponent NNPs by adding single component NNPs and cross-component descriptors. The teaching scheme is to train mono-elemental NNP, with mono-element training sets, to get the first set of NNP parameters. Then, taking two mono-elemental NNP and train it, with a mixed training set, but this time just adjusting the mixed biases and weights. Finally, the third mono-elemental NNP and trained mixed NNP are used, with a full-mixed training set, fixing the old weights and biases. Following this idea it is reasonable to think that more components can be added to the mix, but the computational cost also increases, and it is not guaranteed that the used descriptors would provide enough information to the NNP. These types of potentials can be seen as a middle point between DFT and interatomic potentials because they get a precision close to DFT and using just atomic positions in the same way that interatomic potentials do. But, the reader has to be aware of their drawbacks too. Machine learning algorithms are great interpolators in general, but awful extrapolators, i.e., they know how to solve things that are not too off, concerning the training set. It is also important to notice that NNP, even if they have a lower cost compared to DFT, are not as fast as interatomic potentials. This higher computational cost makes big system size calculations, like those above 1000 atoms, to be impractical to perform with some techniques that will be covered in the further section.

1.3 Searching methods

With the correct interaction potential chosen, it is possible to start to look for viable nanostructures. This raises an important question: What is a viable nanostructure? A sustainable structure will be the one that is capable of existing for a reasonable quantity of time, and minimum energy structures meeting that condition. The challenge with this issue is that the number of possible configurations grows exponentially with the number of atoms in the system, and then the computational cost to find a specific structure increases too. This high computational cost forces the use of highly efficient methods to explore all possible structures, which will be called the configuration landscape from now on.

In these kind of problems, stochastic–heuristic minimization methods have been used for different applications.[52] These methods are used because they allow to solve the optimization problem, or to find minimum energy structures for our purposes, without prior information.

In this section, four optimization methods will be discussed: basin-hopping, genetic algorithm, minimal hopping and annealing. The first two methods are based on applying significant modifications to the structures, while the last ones use small structural changes. This and other characteristics will be discussed in this section to select the most convenient approach to use in systems with a large number of atoms.

1.3.1 Basin hopping method

Basin-hopping [53] is one of the most unbiased methods among all others presented in this work. This technique forces random changes in the structures and then applies a deterministic minimization process, such as conjugate gradient. The new structure is accepted using a Boltzmann distribution over the energy difference between the generated structure and the previous one ($\Delta E = E_{new} - E_{old}$),

$$e^{\frac{\Delta E}{\alpha}} > \text{RND}, \tag{1.14}$$

where RND is a random value between 0 and 1, and regulates the acceptance of higher energies. The whole process looks like little bounces between local minima; that is where the name of this method comes from.

The major strengthen of this technique is also its biggest flaw, which is its unbiased nature. Basin-hopping uses very little system information to keep itself unbiased, relaying actively in trial and error to achieve its goal. The heavy use of trial and error leads to a significant performance drop for bigger sizes, as has been reported when multiple sizes calculations are performed [54], but it does not tend to skip any configuration given enough time.

1.3.2 Genetic algorithm

Genetic algorithms (GA) are inspired by biological evolution and natural selection. The core of these types of algorithms is to generate an offspring population from a set of parents and then select the best members among both of them using a fitting function. It is vital for these GAs to modify the offspring generation enough to get significant differences while keeping those changes viable. Among all the transformations implemented, the most used is mating [55], because it brings the possibility to pass the best features from the parents to the offspring. As in nature, the mix of population diversity, given by deviant broods and environmental pressure provided by selecting the fittest elements every generation, address the search towards the global minimum.

The performance of these type of algorithms depends heavily on their offspring generation to explore the configuration landscape. The correct production of offspring gets more difficult as the cluster size increases and can present problems by skipping odd shapes that modification operations are not made for.

1.3.3 Minimal hopping method

Minimal hopping method follows the same idea as basin-hopping but uses molecular dynamics instead of random displacements to look for new local minima. The use of molecular dynamics guides the search trough PES with small displacements each timestep. The molecular dynamics procedure uses a random initial velocity with fixed kinetic energy associated with it; then the simulation is performed until a new potential well is reached.[56] Another difference is that this algorithm does not use the same acceptance criteria, here the new structure is accepted if it was not visited before to guide the search in new sectors. The reject of a structure implies an increase in kinetic energy, and acceptance will reduce it. The use of these constantly increasing and decreasing kinetic energies narrow the escape routes using the minimal hopping path, which will be more likely to get lower minima according to Bell-Evans-Polanyi principle.[57]

The minimal hopping approach can perform more efficient searches than the evolutionary algorithm in force calls and successful runs [58]. The scalability of the algorithm is still an issue because the problem that implies differentiate two structures for a large number of atoms. For example, in Goedecker's original work [56], energy differences are used to judge the difference between the two structures, but these differences can get neglectable when the number of atoms increases. This difficult distinction and the historical comparison can trap the algorithm and force it to increment kinetic energy into a point of failure, destroying non-periodic structures.

1.3.4 Annealing method

Annealing is a heating and cooling technique, which can be performed by molecular dynamics or Montecarlo methods. The scheme of this algorithm is simple: first set the system at a stable fixed temperature. Then cool down the system, and repeat until the energy of the system gets stable. The Montecarlo approach to annealing, also called simulated annealing [59], stabilizes the system by randomly changing parameters (atom positions) and then accepting these changes when the following test passes:

$$e^{\frac{\Delta E}{k_B T}} > \mathsf{RND} \tag{1.15}$$

with RND a random number between 0 and 1. This test became expensive for large systems because of the large high energy states that the system can fall into (atom collision), getting many rejections on them. On the other side, the molecular dynamics approach avoids these atomic collisions because the equations of motion get the system away from them. But, while this approach does not get failed moves, it can take long simulations to explore a significant portion of the configuration landscape.

These annealing methods are pure brute force algorithms. They guide the system without any external information but the system interactions. The lack of any external deviation makes the annealing approaches theoretically robust and simple, which makes them a perfect baseline to get a basic performance.

1.4 Summary

In this chapter, different interaction potentials and optimization techniques were revisited within discussing their advantages and disadvantages, which will be weighted in this summary. The main perk to emphasize is efficiency because of the large number of atoms involved in experimental size systems require a significant amount of computational resources.

The efficiency of interaction potentials considers accuracy and computational cost. Accuracy plays a fundamental role in the correct representation of the atomic element in simulations, so it has to be as high as possible. Even though, compromises have to be made to get optimal results for large atomic systems. The first discarded method has to be DFT due to its impractical computational cost at larger sizes, i.e., due to its poor scalability. Then, only ANNs and EAM are left as viable options. ANNs are more precise than EAM and have the same linear scalability, but their development is still in early stages, which means that they will require more work to be implemented efficiently in the systems of interest. Because of these reasons, EAM potentials are chosen, despite the promising results that ANNs can give in further works.

In optimization techniques, efficiency is inversely proportional to the computational time to get the minimal configuration. The key to get the best efficiency is to visit new minima in the least number of steps. This task is a problem for totally unbiased routines, such as basin-hopping. Genetic algorithms are very effective routines for low sizes, due to their capability to keep useful information from different minima, but their effectiveness drops drastically as size increases. Then, minimal hopping and annealing methods remain as viable options because of their local exploration capabilities. These localized optimizations strongly rely on their initial configurations; thus, they are not affected as significantly as basin-hopping and genetic algorithms by the bigger size of the configuration landscape. Finally, the efficiency of minimal hopping against annealing will depend on the complexity of the configuration landscape. However, annealing offers a more robust procedure to implement a novel method, which will be described in the following chapter.

In summary, EAM potentials and annealing techniques are the ideal choices to optimize large atomic system configurations due to their efficiency and simplicity. Also, there are promising alternatives to improve the performance and accuracy using ANNs and minimal hopping techniques, but their complexity does not allow an efficient implementation, so they are suggested for further work.

Chapter 2

Bimetallic nanoparticles

To find stable structures of nanoparticle systems is an immense challenge, in part because the number of local minima increases exponentially with the number of atoms. In fact, Frank Stillinger demonstrated this exponential growth for interacting entities [30]. All these local minima can lead to different shapes that may imply different properties, as it was previously reported in several publications [60, 61, 62]. When considering bimetallic nanoparticle properties, it is not only important to consider the shape of the particle, but also their components and elemental distribution. This new degree of freedom opens the possibility of more isomers to appear and possibly coexist in different environments. In the following section, we propose a method that allows to focus on smaller regions of interest to obtain viable configurations for large-scale atomic systems.

2.1 Design of large nanoparticle systems

In the previous chapter we exposed different methods to explore the configuration landscape but all of them struggle to find a minimum when the system grows. The size issue is understandable because of the exponential growth of the configuration landscape. The most straightforward answer to this issue is to constrain the search around a good first guess.

2.1.1 The energy of a good first guess

A good first guess must be a configuration as close as possible to the global minimum, with a fixed number of atoms. Therefore, it is necessary to sort out the most significant energy contributions for the entire system in a simple way. These energies can be separated into three types for any large enough system: bulk (E_B^j), exposed surface (E_S^j) and interface surface (E_I^j) energies.

The exposed surface and interface surface energies are thought as the energy difference between the isolated bulk structures ($E_B = E_B^{T1} + E_B^{T2}$) and the bimetallic nanostructure (E)

$$\begin{aligned} E - E_B &= E_S + E_I \\ E - (E_B^{T1} + E_B^{T2}) &= (E_S^{T1} + E_S^{T2}) + (E_I^{T1} + E_I^{T2}) \\ E &= E_B^{T1} + E_B^{T2} + E_S^{T1} + E_S^{T2} + E_I^{T1} + E_I^{T2}. \end{aligned} \tag{2.1}$$

Now the energy has to be related to the geometrical configuration (see Figure 2.1). The simplest approach possible to this issue is to take a segregated system, where it is possible to easily define boundary regions for each element (T1 and T2). This way, the bulk energy can be related to their number of atoms (N_j) and the surface energies to their surface areas (A_I^j and A_S^j)

$$\begin{aligned} E_B^j &= N_j \varepsilon_j \\ E_{I/S}^j &= A_{I/S}^j \sigma_{I/S}^j \end{aligned} \tag{2.2}$$

therefore, system energy can be simply expressed as

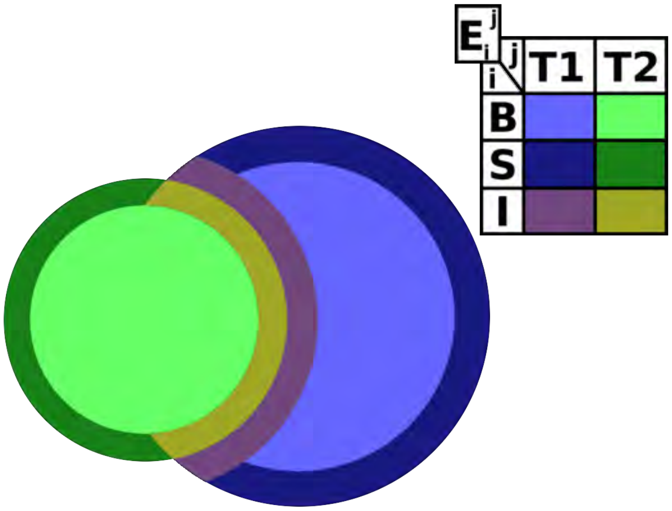

Figure 2.1: Schematic cross-section of a nanostructure with colored zones symbolizing different energy contributions E_i^j in equation 2.1. The color symbology is described in the table for i=B,S,I and j=T1,T2.

$$E = N_{T1}\varepsilon_{T1} + N_{T2}\varepsilon_{T2} + A_S^{T1}\sigma_S^{T1} + A_S^{T2}\sigma_S^{T2} + A_I\left(\sigma_I^{T1} + \sigma_I^{T2}\right), \tag{2.3}$$

where ε_j and σ_j are the energy per atom and energy per surface area unit respectively. Since morphologies are the only ones considered to minimize the energy in equation 2.3 (N_{T1} and N_{T2} are fixed), it is safe to ignore the first two terms that are not dependent on the system surfaces. The next two terms are in equation 2.3 are exposed surface energies, which increase system energy as their respective exposed surface area increases ($\sigma_S^j > 0$). The last term represents the interface surface energy, whose energy density (σ_I^j) particular values may differ case by case. For the particular case of segregated arrangements, the condition

$$\sigma_I^{T1} + \sigma_I^{T2} > 0, \tag{2.4}$$

is mandatory because it represents systems that reduce interface area, effectively separating the involved elements.

The simplifications presented in equation 2.3 reduce the selection pool to spherical shapes that reduce exposed surface and interface surface areas. In the experimental review made by Ferrando et al. [12], these "nanoalloys" were classified in three segregated categories or mixing patterns: core-shell, subcluster (also known as Janus structures) and multishell. The former two are segregated structures that satisfy $A_S^{T1/T2} = 0$ and $A_I \to 0$ in the simplified energy model of equation 2.3, which may minimize the energy of the system. These extreme conditions, and their possible proximity to a minimum, make core-shell and Janus configurations the perfect candidates as segregated first guesses. In the case of multishell structures a significant increase of the interface area exist, which does not minimize the energy, therefore is discarded as a good first guess.

In mixed or alloy structures there is not a clear interface between both elements in the nanoparticle. Even though, it is possible to consider the alloy as a new material with the structure of a known bulk alloy. This approach makes possible to consider alloy nanoparticles with the same motifs as segregated ones but, in this situation, the involved material can be defined as a stable mix of both atomic elements.

Based on all previous statements, the proper first guess structures have core-shell or Janus motifs with materials that can be single-metal or metallic alloys, which will be used as initial structures for the following optimization routines.

2.1.2 Optimization of large atomic systems

Once the good first guesses are taken, the search is now closer to the goal, but this may not be enough. The problems that optimization algorithms have for large systems are still present and must be addressed first. Among all the methods presented in chapter 1, the most benefited with this good first guess is annealing with molecular dynamics because its biggest flaw is the poor exploration performance. This great performance benefit along with the unbiased essence and simplicity of the method are the reasons

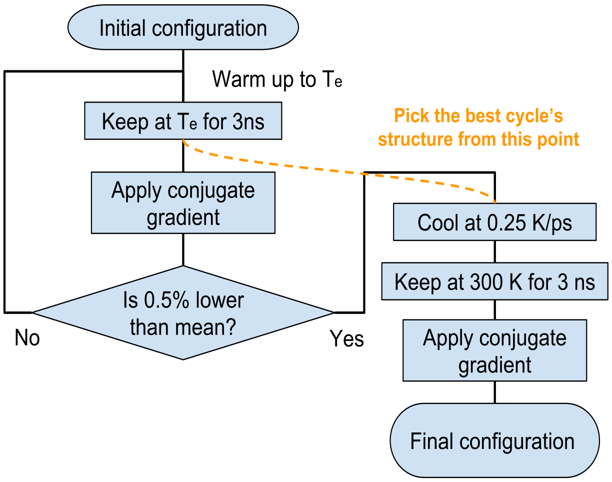

Figure 2.2: Cycle annealing diagram

why this algorithm is selected as a first option to work with. Let us start digging deeper into how molecular dynamics annealing works.

All performed simulations will be done using the LAMMPS software [63]. The system is simulated in an NVT ensemble at a constant annealing temperature T_e. Thermodynamically a higher T_e means higher entropy, which means that the system will have available a wider set of configurations to explore. High entropy appears like an excellent condition to explore many arrangements as possible, but this also means that the system will be able to get stuck in high energy local minima. In contrast, low temperatures will not allow the system to explore the configurational space in reasonable simulation time. Therefore, a working T_e range must be set to avoid unnecessary higher entropies and enabling the nanoparticles to move on low energy paths. A possible T_e range corresponds to a semi-melting phase, where only the surface atoms have high mobility.

Even though stable states tend to trap molecular dynamic simulations, it is still possible for simulations to escape from these potential wells. An annealing search must be divided into shorter cycles to enforce the visit candidate states, which could be missed

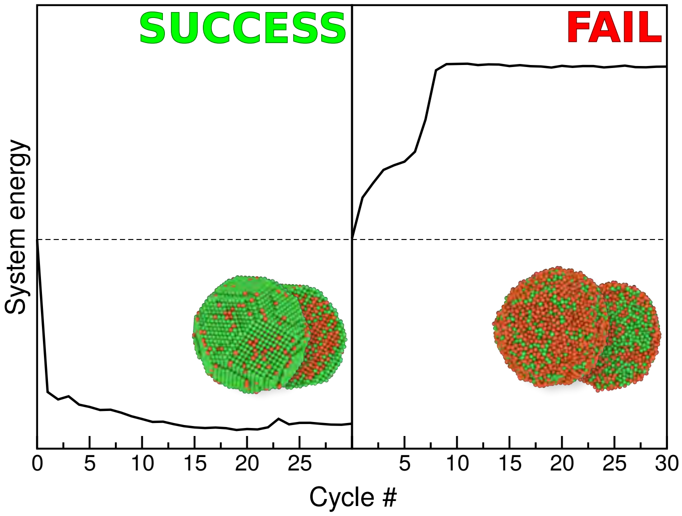

Figure 2.3: Examples of successful (left) and failed (right) molecular dynamics annealing cycle energies. The segmented line defines the energy of the initial configuration. Inside each plot, example structure results are shown with their complete form in front of their cross-section.

otherwise. In each cycle, the structures are thermalized at T_e for a long simulation time (3 ns), and then relaxed using conjugate gradient method. The energies for every relaxed configuration are stored to monitor the progress of the optimization. Successful optimization simulations show a consistent energy reduction as they approach to a minimum (Figure 2.2a), while failed ones quickly rise their energies up to a plateau where they reach the melted state (Figure 2.2b). When these series of annealing cycles are incapable to reach any lower energies than the mean of the last 10 cycles (within a 0.5% tolerance), a final cooling process is performed to reach the lowest point of the surrounding explored configuration landscape. This final cooling begins before the conjugate gradient is applied to the lowest energy cycle and is cooled at a ratio of 0.25 K/ps from T_e to room temperature (300 K). Then the structure is left at room temperature for 3 ns before a final conjugate gradient is applied to get the final structure (see Figure 2.2).

The annealing cycle strategy works for single element clusters because all atoms in the structure share the same properties, but this is not the situation for all bimetallic configurations. The differences between elements often cause that the semi-melting range does not coincide, which means that a single optimization process may not be optimum for bimetallic systems. A two-step optimization process is proposed to solve this issue. The first step is to optimize spherical cuts of known crystalline lattices from both involved materials, which includes alloy materials. Melting temperatures are determined using Lindeman indexes [64], which are obtained from a short heating simulation. Then, the temperature T_e is set around 80% of the obtained melting temperature to fall around the lowest section of the semi-melted region. Later, optimized configurations are used to build core-shell and Janus motifs. Core-shells are built with an optimized core surrounded by a spherical shell cut of the opposite material's crystal lattice. In the Janus case, both optimized structures are put next to each other. Finally, a second melting temperature measurement and optimization routine is applied to the newly generated configurations.

The two-step routine generates an optimized configuration for each initial first guess. The lowest energy structure is then chosen as the stable result of the search. The combination of these optimization routines results in a robust search around possible arrangements, which could be comparable to synthesized samples.

2.2 Application on real systems

Real systems are usually considered as nanoparticles with sizes large enough to be synthesized in experimental procedures. Therefore, the size of these arrangements is often over 1000 atoms, which implies a great optimization challenge as it was commented previously.

In this section we will search for stable atomic configurations following a simulated annealing approach, based on specific initial guesses. In the first case we will study the stable configurations of FeCu, FeNi and AgCu particles as a function of their concentration and sizes. Then, some conclusions about the results are given and possible new directions and applications for this work are envisaged.

2.2.1 FeCu

FeCu bimetallic arrangements are the first to be addressed in this chapter. In these nanoparticle systems there is only segregated configurations, due to the fact that these elements are immiscible [65]. Therefore, the initial structures will be built with Fe and Cu crystalline stable structures, which have body centered cubic (BCC) and face centered cubic (FCC) lattices respectively.

The study is guided towards the effects of Cu concentration over Fe nanoparticles [66]. It is useful to separate particles in three sizes, depending on the number of Fe atoms contained in each one. The first category contains 6183 Fe atoms ($\sim$5 nm diameter) and is called the "small" size. The second one contains 15473 Fe atoms ($\sim$7 nm diameter), denoted "medium". The last one contains 32743 Fe atoms ($\sim$9 nm diameter) and is called the "big" size. For these sizes, concentrations of around 10, 20, 30, 40, 50, and 70% were considered by adding different amounts of Cu atoms to the Fe NP. For example, at small sizes, we used 791, 1710, 2490, 4178, 6092, and 14579 Cu atoms, respectively; while for medium sizes we considered 1832, 3788, 6794, 10526, 15448, and 36096 Cu atoms. Finally for big sizes, we used 3780, 8780, 14054, 21968, 32530, and 76542 Cu atoms, respectively.

In this particular scenario the interaction potential was modeled using an embedded atom method potential, whose parameters are taken from the work of Bonny et al. [67]. This potential offers a good description of elastic properties, diffusion dynamics, and thermal transport coefficients [68].

Structural configuration of FeCu nanoparticles

A summary of the structural configurations found for energetically optimized FeCu NPs is shown in Figure 2.5a, with a cross-sectional view of the atomic structures, as a function of the size and Cu percentage (Figure 2.5b), where we have identified three characteristic Cu percentages (I: 10%, II: 40%, and III: 70%). At the low Cu percentage (10%), we can see that Fe atoms (brown spheres) are mainly arranged as a compact particle, whereas Cu atoms (green spheres) are distributed around the Fe core. At 70% of Cu, the structure is basically segregated, with two joined monoatomic clusters. Finally, at 40% Cu, we observe a CS morphology for small particles, while a JN-like structure is obtained for medium and big NPs. From our results, a CS to JN-like stability transition is observed as Cu is increased, this transition being slightly shifted to the left for big particles. This transition can be associated with the energy of Fe–Cu interactions that decreases after a maximum value is reached (e.g., 30% Cu at big particles, see figure 2.4), which means that a segregated structure becomes preferred over CS morphologies as the Cu content increases.

Once we have determined the preferred morphology of the bimetallic particles at different Cu concentrations, the crystalline phases of the selected cases are reported. These phases are obtained from the common neighbor analysis (CNA) performed by the scientific visualization tool OVITO [69]. Figure 2.5c depicts the presence of mainly two crystalline phases: bcc (blue) and fcc (green) lattices, with light gray particles related to the atoms at the surface or defects. At 10% Cu, CNA shows only the bcc phase for all sizes. At 70% Cu, there are two phases: bcc phase for Fe and fcc for Cu. Finally, at 40% Cu, we can see that the NP shows mainly a bcc phase for Fe, while Cu is mainly ordered as an fcc lattice. Additionally, we can observe atoms associated with hexagonal closed-packed (hcp) structures (red) because of twins (single red planes) and stacking

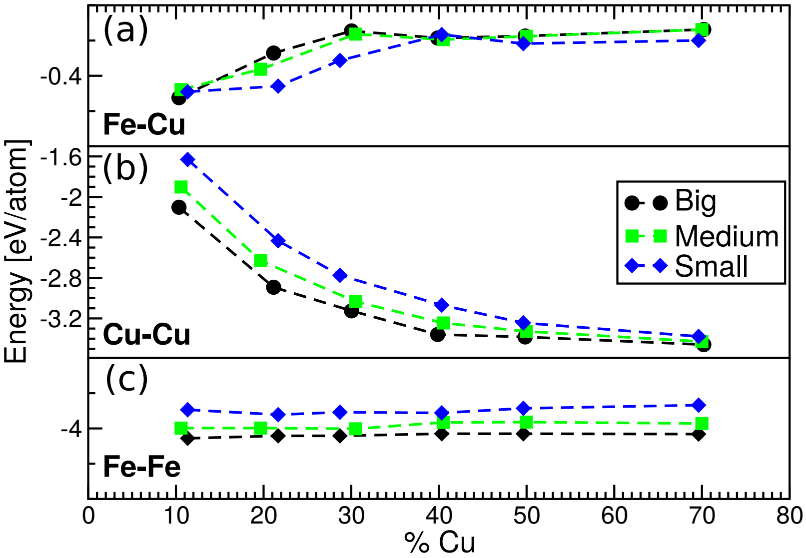

Figure 2.4: Energy of optimized FeCu particles at different Cu percentages. The energies were separated considering only (a) Fe-Cu, (b) Cu-Cu and (c) Fe-Fe interactions.

faults (SFs, double red planes) nucleated at the Fe–Cu interface.

To consider the coordination analysis of the optimized NPs, the radial distribution function (RDF), g(r), is calculated and shown in Figure 2.6, for stable systems at 10, 40, and 70% Cu. Here, we can see the coordination per element (brown and green lines for Fe and Cu, respectively) as well as the total RDF (red line) at different sizes. At the low Cu percentage, both Fe–Fe and the total RDF give the expected peaks of the bcc lattice (crystalline bcc peaks are depicted as segmented black lines), and even Cu–Cu shows a similar distribution of peaks. In contrast, at 70% Cu, the total g(r) reflects the contribution of both bcc and fcc lattices associated with Fe–Fe and Cu–Cu, respectively (crystalline fcc peaks are depicted as dotted black lines). At 40% Cu, we have mixed results, where smaller NPs show mainly bcc lattice peaks, whereas medium and big NPs have the formation of both bcc and fcc phases. These results can be directly related to experimental diffraction results and lead us to expect a bcc phase of Fe at low Cu

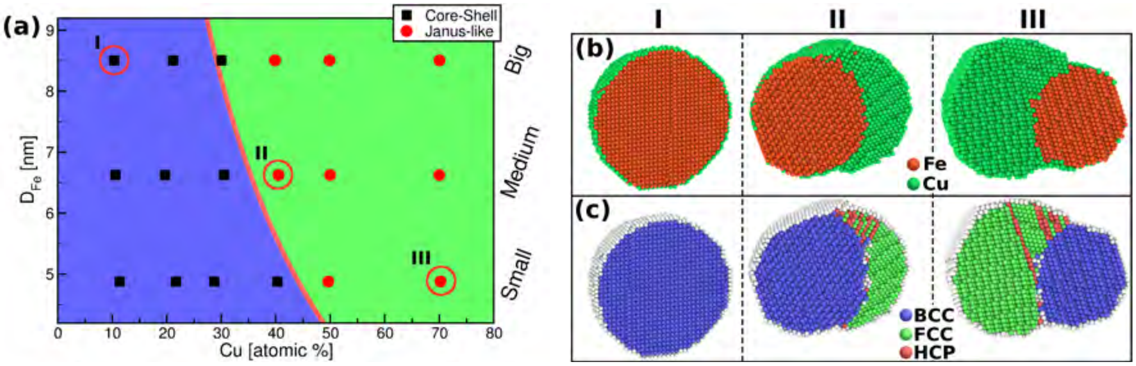

Figure 2.5: (a) Cluster structure as a function of size and Cu concentration. The pink line depicts the CS to JN-like stability transition from the continuous model. Cases I, II, and III are shown at the right side. Cross-sectional views of FeCu particles encircled at (a), showing elemental composition (b), and structural defects (c). In (b), colors follow represent Fe (orange) and Cu (green) atoms, and in (c), atoms associated with the hcp phase (twins and stacking faults) are shown in red, whereas particles without any associated phase are shown in light gray.

concentrations, while bcc and fcc phases are expected at high Cu concentrations.

Stress and surface energy

Figure 2.5c shows that minimized NPs exhibit structural defects in Cu. Because Cu has a low SF energy, [68] surface nucleation of SFs might be expected, as it has been reported for solid NPs [70] and nanowires [71]. Also, the accumulation of SFs leads to nanotwins [72]. These low-energy planar defects are not expected to contribute significantly to global structural transitions. A twin boundary is a sigma-type grain boundary, and Suzuki and Mishin have shown that interstitial diffusion across and along Sigma-type grain boundaries has lower activation energy than bulk diffusion [73].

Figure 2.7 shows the final relaxed configuration, with dislocations and the surfaces of the Cu and Fe NPs, for the small case, and 50% Cu. There is one twin boundary, seen as a single plane of defective atoms, and two SFs, seen as double layers of atoms. Additionally, from Figure 2.7, it can be seen that the Cu atoms wrap around the external

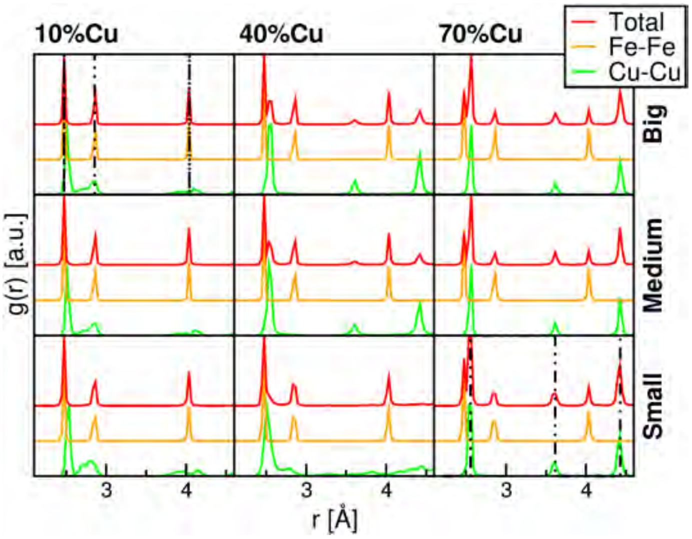

Figure 2.6: Total and partial RDF of FeCu particles as a function of the Cu concentration and size. Segmented and dotted lines correspond to three first peaks of the crystalline bcc and fcc lattices, respectively.

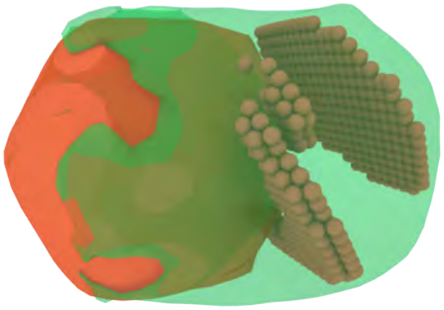

Figure 2.7: (a) Defects for the small (5 nm Fe core) FeCu particle at 50 % Cu, after relaxation. Stacking faults (double plane) and twin boundaries (single planes) are depicted with brown spheres. Cu envelops the red Fe cluster, leaving only a relatively small portion of uncovered Fe.

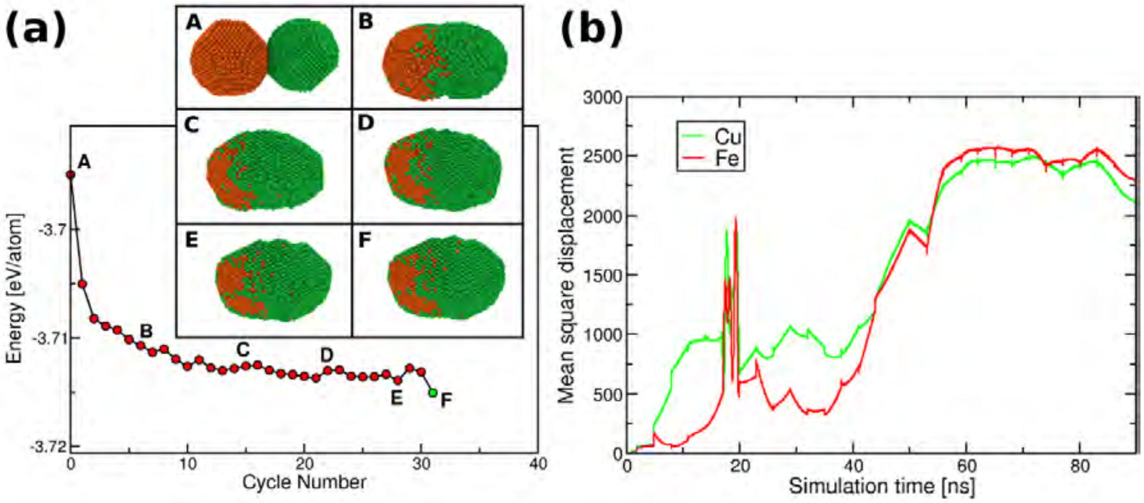

Figure 2.8: (a) Energy of small JN nanoparticle at 50% Cu during the optimization process. The final step F corresponds to a slow cooling process at the end of optimization. (b) Mean Square Displacement during the optimization for Fe and Cu atoms.

surface of the roughly spherical Fe NP, leaving out only about half of the Fe surface and generating a Cu surface significantly larger than the initial Cu one, and resulting in an enhanced Fe–Cu interaction. Additional information is given in Figure 2.8, showing the energy optimization and depicting some structures during the optimization process until the final configuration (F case in Figure 2.8a), while the mean square displacement shows a higher diffusion of Cu atoms. A similar behavior occurs for other cluster diameters and concentrations above the stability transition of CS and JN.

There are no important defects observed in Fe. This is expected, given that the nucleation stress for dislocations is roughly proportional to the shear modulus of a given material, [74], and in Fe, the value is 116 GPa, [75] which is significantly larger than that in Cu (76 GPa) [68]. For Fe nanowires, twins have been observed only for stress above 20 GPa [76], which is much larger than that in the annealing process.

SF nucleation can occur from surface imperfections [77] but in our simulations it is generally triggered from the Fe–Cu interface, where stress concentration can occur during annealing. Nucleation leads to stress relaxation, and the interface is nearly stress-free, unlike what happens for semi-infinite planar interfaces [78].

Planar defects can strengthen the NPs [79]. However, planar defects observed in our simulations are not stable and do not survive to one high temperature annealing cycle to another. SF recovery has been observed in nanocrystalline metals, [80] and detwinning can occur when surfaces are present [81]. Under room-temperature conditions, defects might survive and change mechanical and optical properties of the NPs [82].

Experimental evidence of FeCu bimetallic nanoparticles morphology

Our simulations and model were compared with the experimental results obtained by Pamela Sepúlveda and Nicolás Arancibia at Universidad de Santiago de Chile.[83, 66] The synthesis of FeCu bimetallic NPs, that targets two different proportions of Cu in the structure (10% Cu and 50% Cu), was performed using the simultaneous reduction chemical method and the experimental procedure reported by Wang and Zhang [84] and Xiao et al., [85] obtaining a black material corresponding to bimetallic NPs. Figure 2.9 shows the scanning transmission electron microscopy (STEM) analysis and energy-dispersive X-ray spectroscopy (EDS) line profile of the particles in both nanomaterials. The profile for 10% Cu (Figure 2.9a) displays the presence of mainly Fe particles with low amount of Cu around Fe, associated with the formation of oxide and CS structures. In contrast, for the case of 50% Cu, Figure 2.9b,c, displays two types of NPs, corresponding to separate Cu and Fe NPs, respectively. These results are consistent with theoretical and modeling studies, finding that a low Cu proportion promotes a CS structure, while the increase of the "noble metal" concentration in bimetallic structures generates an evolution of the morphology of these particles, with the preference of segregated structures (JN-like) at 50% Cu, suggesting that there would be a critical number of Cu atoms before

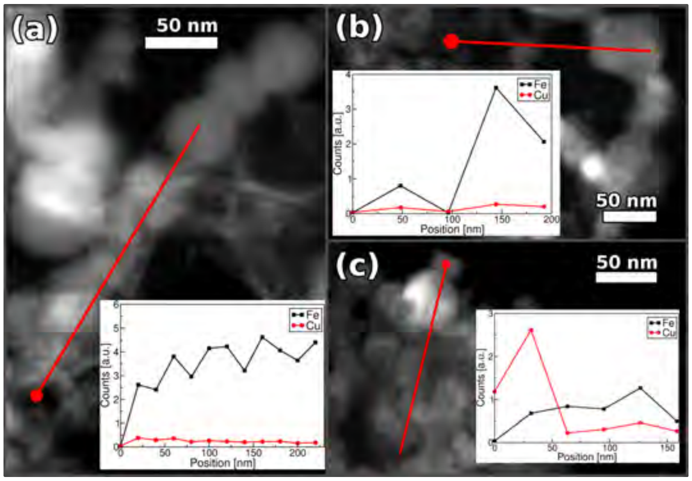

Figure 2.9: Linear mapping of the synthesized bimetallic NPs for (a) 10 and (b,c) 50% Cu, respectively. Initial position is defined with the red circle in the red line. (a) suggests a CS structure, while (b,c) suggest segregated or JN-like structures. Image obtained thanks to the collaboration with P. Sepúlveda and N. Arancibia

the stability transition from CS to other structures begins. This segregation has already been reported by Xiao et al. [86], finding a separation of Fe and Cu after the synthesis of bimetallic NPs.

This concentration-dependent morphology also played a key role in Fe–Cu As sorption capacity [83], where low concentration morphologies (core-shell) achieved better performance over higher concentration samples (Janus) and pure Fe nanoparticles.

Conclusions

We studied the morphology of FeCu NPs by using a multistep optimization procedure, establishing Cu concentration conditions where CS or JN-like structures are the more energetically stable morphologies. At low Cu concentrations, Cu atoms wrap the Fe cluster following the Fe bcc lattice. Once we increase the Cu concentration, the shell of Cu atoms shows an fcc lattice until the stability transition point from CS to JN is reached. A segregated structure is obtained at high Cu content, with a bcc lattice for

Fe and an fcc lattice for Cu. The Cu–Cu energy becomes more important as the Cu percentage is increased, while the Fe–Cu energy grows quickly until the first monolayer is built, and from there on forward, it has slow-paced growth as the Cu content increases. This effect leads to a stability transition point where it is more energetically expensive to surround the Fe core than to segregate the Cu atoms. Nevertheless, we expect the CS to JN stability transition behavior to be observed for other materials and help to design bimetallic NPs at requested conditions, as a function of the elemental concentration. In this direction, future work might also consider other bimetallic NPs of technological interest, [21, 87] as well as the incorporation of iron and copper oxide compounds. Finally, a continuous model for the immiscible FeCu system is proposed to obtain the most stable configuration, resulting in a structural map in agreement with molecular dynamics simulations and experimental evidence. This model can be used to analyze the structure of other NPs, provided the characteristic energies are calculated from atomistic simulations. Tailoring of certain structures for a given size and composition would also allow the possibility to engineer desired properties for technological applications.[21, 10]

2.2.2 AgCu

AgCu systems lack alloy motifs at bulk sizes.[88] In this context, silver (Ag) and copper (Cu) binary NPs needs to be highlighted, because of the interesting motifs that they can take at nanoscale,[89] leading to potential applications controlled by morphology or concentration of these NPs. For example, among the metallic nanomaterials, Cu NP is an excellent option because of their low-cost production and useful catalytic, optical and electrical properties.[90] However, it is well-known that this kind of nanomaterial is unstable in air, which limits its application range. Therefore, to prevent the oxidation of CuNPs, Lee et al.[91] synthesized CuAg core-shell NPs, which displayed enhanced oxidation stability and electrical properties. These architecture NPs were further used to prepare conductive ink. In another study, Shin et al.[92] investigated Ag NPs and AgCu alloys and core-shell nanostructures as a catalyst for oxygen reduction reactions through density functional theory. The authors found that AgCu alloy seems to be the best candidate to perform the mentioned reaction, even if it is more energetically unstable than AgCu core-shell nanostructure. This study of Cu–Ag nanoparticles systems is focused in the synthesis process of these nanostructures and how different concentrations affect the final morphology results. In order to get the morphology for the different concentrations, theoretical modeling will be used to find the most stable configurations at different concentrations and sizes. The study is done in a similar way to Fe–Cu nanoparticles. Annealing optimization techniques were applied over a Cu–Ag system. The interactions were modeled using an EAM interaction potential with parameters fitted by Williams et al.[93], which has been used in the study of mechanical properties of CuAg structures.

The nanostructures considered for this study are six structures, which are small and large arrangements of 4213 (~ 5 nm diameter) and 10000 atoms (~ 6.5 nm diameter) respectively, with concentrations of 10% 50% and 90% of Cu. Since, there are not miscible bulk phases for this system [88], only segregated structures are considered. The segregated structures considered for this study follow the motifs presented in section 3.2; which are all possible core-shell configurations, such as Cu core with Ag shell (Cu@Ag) and vice-versa (Ag@Cu), and the Janus configuration.

Optimization results

After the optimization over all initial configurations, different energies were obtained for the final structures, which are showed in the table 2.1. These energies show that core-shell initial configurations reach the lowest energy states for all cases, except for 90% Cu concentration. In this particular concentration the morphologies of core-shell and Janus initial arrangements reach similar morphologies, which are categorised as core-

Table 2.1: Cu-Ag energies relative to lowest energy configuration

Energy difference(meV/atom)				
N	Cu %	Cu@Ag	Ag@Cu	Janus
4213	10	0.00	4.07	7.74
	50	0.00	12.67	9.13
	90	0.39	25.00	0.00
10000	10	0.00	8.84	1.94
	50	0.00	17.35	3.08
	90	0.62	25.67	0.00

shell structures because of the core-shell segregation presented by the elements involved (see figure 2.10). In the table 2.1 is worth notice that core-shell Cu@Ag and Janus initial structures reach configurations with lower energy differences as the size increases, contrary to the energy difference increase in Ag@Cu.

Figure 2.10 shows the different morphologies for the lowest energy structures along all concentrations and sizes. The atom distributions in all the structures involved show a core-shell distribution with Cu located in the core. This includes the structures with a 90% of Cu, which used Janus structures as initial configurations, therefore Janus CuAg nanoparticles are not stable at high Cu concentrations. In other concentrations all configurations are clearly differentiated. This differentiation is still present at low Cu concentrations, where energy differences are considerably low and get lower with the larger size, therefore the result suggest that core-shell and Janus stable structures may exist at bigger sizes.

The structural differences between core-shell and Janus structures found are shown in figure 2.11. In this figure can be seen a cross-section and a heat map with the elemental distribution of Cu and Ag in the large nanoparticles with 10% and 50% of Cu concentration. The main morphology differences that can be seen in core-shell and Janus structures are the elemental distribution and Cu shape in the nanoparticle. These

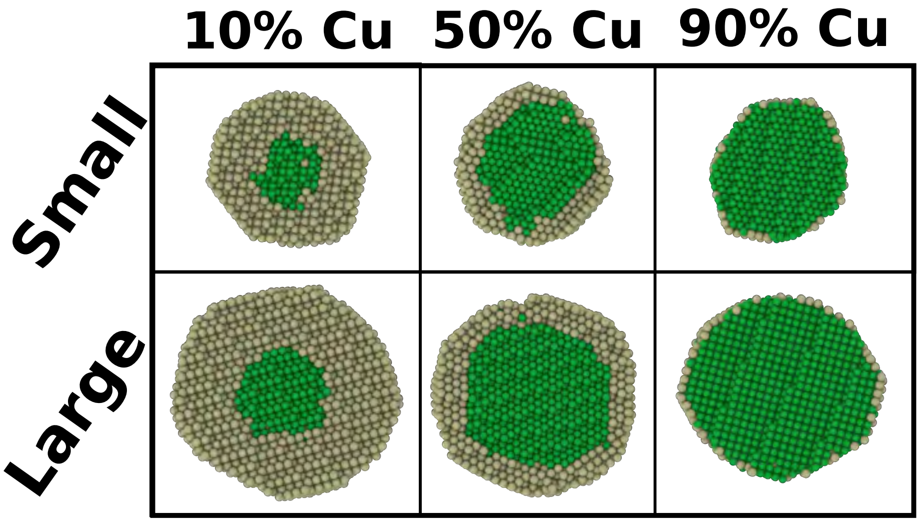

Figure 2.10: Cross section of lowest structures along all sizes and concentrations.

shape differences can be seen in the Janus structures, where Cu present a less spherical distribution than core-shell Cu cores, while is still covered by a thin silver layer.

The structures obtained in CuAg nanoparticle systems prefer the formation of Cu motifs coated with Ag, because the lowest structures found involve at least a thing Ag layer surrounding a Cu cluster.

Experiment comparison

Different nanostructures of general formula Ag_xCu_y were synthesized by Rafael Freire at Universidad de Santiago de Chile. The synthesis followed a chemical reduction proccess described by Yu et al.[94] The coefficients x and y denote the theoretical chemical composition, which are 0.1, 0.5 or 0.9. These synthesized nanoparticles were characterized using X-ray diffraction (XRD), transmission electron microscopy (TEM), energy-dispersive X-ray (EDX), selected area electron diffraction (SAED) and high-angle annular dark-field imaging (HAADF) techniques to compare the synthesis with computational results. These characterizations were obtained thanks to the collaborations of Rafael Freire,

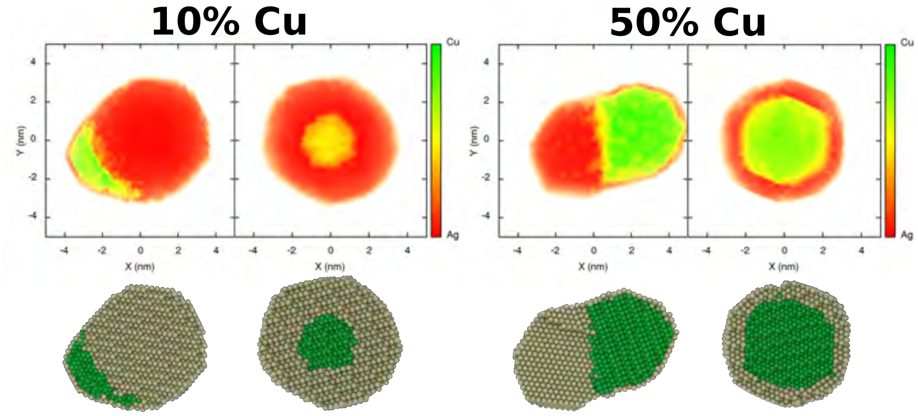

Figure 2.11: Heat map of element distribution for large CuAg nanoparticle systems (10000 atoms) for 10% (left) and 50% Cu (right). Below the heat maps there are cross-sections of their respective nanoparticles.

Loreto Troncoso (Universidad Austral), Ana Laura Elías and Kazu Fujisawa (Penn State University, USA).

The obtained diffraction patterns are displayed in Fig. 2.12(a-c). The black line denotes the observed data (Obs), while the red and blue lines represent the calculated data (Cal) and the difference (Diff) between, i.e. Obs minus Calc, respectively. For all samples, main peaks at 38, 43, 45, 51, 65, 74, 78 and 82Â°. These results suggest the aggregation of Cu and Ag in a face-centered cubic (fcc) crystal structure [95].

In figure 2.12(d-i) are presented the result of TEM and SAED characterizations. The SAED ring patterns evidence the presence of both Ag and Cu fcc crystalline structure in all concentrations. On the other hand, TEM images show different results for each concentration. The 90% Cu (Fig. 2.12d/g) displays an agglomeration of smaller NPs with different contrast and irregular morphology, which suggest the existence of agglomerated Cu and Ag nanoparticles. Once the Cu concentration decreases below 50% of the NPs composition, faceted NPs (Fig.2.12e-f/h-i) can be observed, which indicate the Ag content as the main factor to obtain a regular morphology. According to the literature

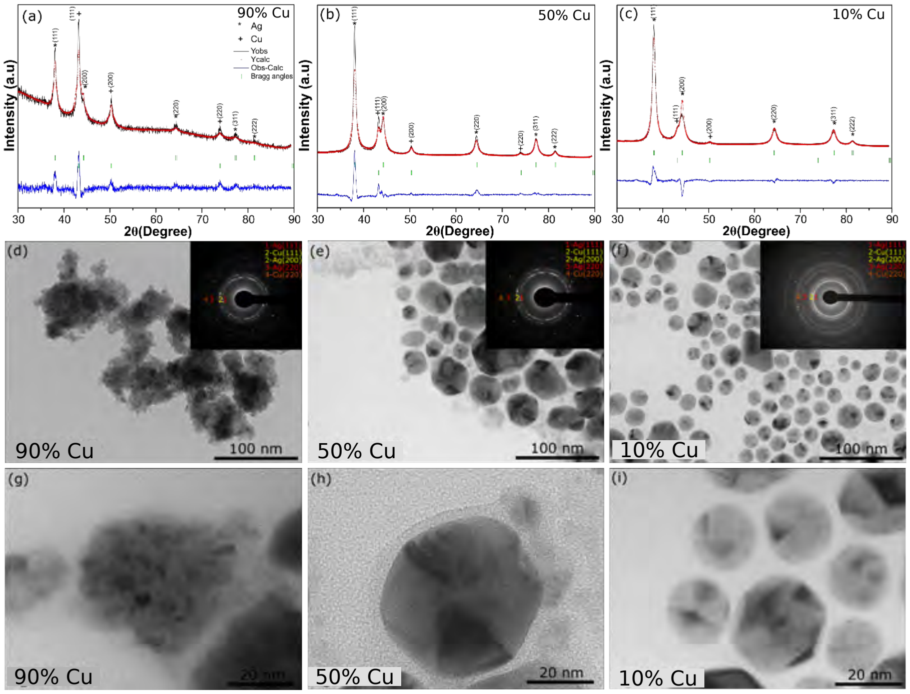

Figure 2.12: XRD pattern obtained for (a) 90% Cu, (b) 50% Cu and (c) 10% Cu. The black and red line denotes the experimental and calculated data, while the blue line represents the difference between them. The vertical green lines correspond to the allowed Bragg reflections; TEM images of the AgCu bimetallic NPs at low (d – f) and high (g – i) magnifications. The identification of each NPs is displayed in the micrograph. The inset om the low magnifications micrographs display the SAED pattern. The images were obtained thanks to the colaboration of R. Freire and L. Troncoso

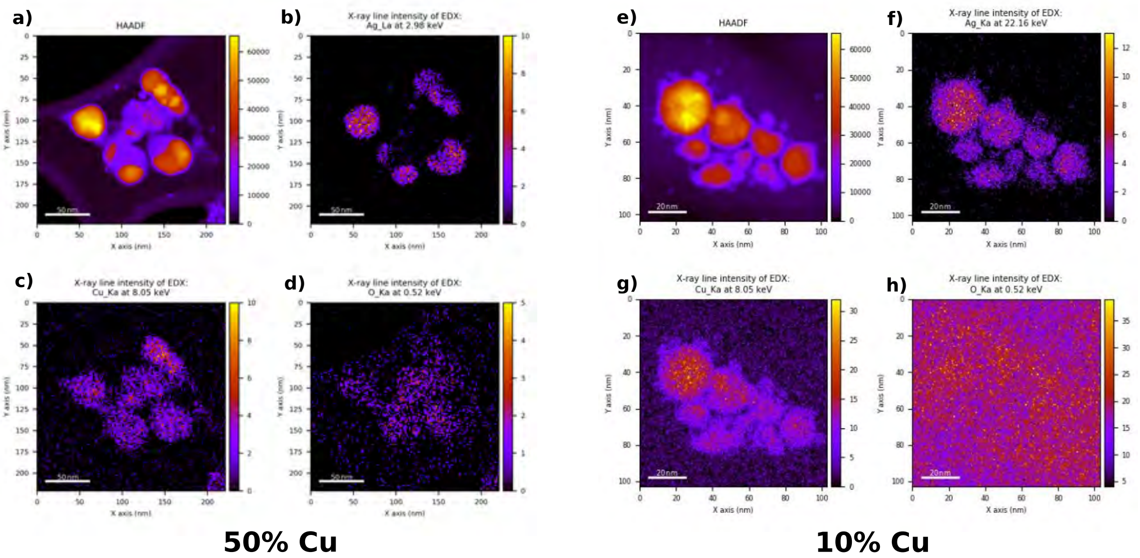

Figure 2.13: HAADF and EDS images over (a-d) 50% Cu and (e-h) 10% Cu samples. Four plots are presented for each sample: (a/e) HAADF, (b/f) Ag-EDS, (c/g) Cu-EDS and (d/h) O-EDS. The images were obtained thanks to the colaboration of A. Elías and K. Fujisawa.

[89] and our simulations, the most stable atomic arrangement for AgCu clusters in the nanometer size range is Cu@Ag. Therefore, in our case, it seems that Ag content is starting to encapsulate the Cu atoms. Although, the encapsulation process was not efficient at 50% Cu, since smaller NPs can also be observed outside the core in Fig.2.12h.

To further identify the elemental composition of nanostructures, HAADF and EDS analysis are shown in figure 2.13 over 50% Cu and 10% Cu samples. For both samples, Ag-EDS shows concentrated spots of Ag. Also, Cu-EDS presents a Cu distribution more segregated in 50% Cu than in 10% Cu. There is also a larger presence of O in the 10% Cu than in 50% Cu sample, which may be due that the latest were taken several weeks before the former. The overall results for these two concentrations present distributions patterns similar to the Janus structures presented in the heat map in figure 2.11, therefore the structures obtained are generally Janus structures.

Discussion

CuAg nanoparticle systems were synthesized and simulated with 10%, 50% and 90% Cu concentrations. Our theoretical simulations presented core-shell configurations as the most stable for all concentrations in the nanoparticle systems. Even though, Janus structures were found as close candidates, which energies got closer to core-shell configurations as their size increases. On the other hand, synthesized results showed dispersed nanoparticles for 50% and 10% Cu concentrations under TEM measurements. The XRD and EDX analysis confirmed the bimetallic composition of the structures. Additionally, EDX analysis showed elemental distribution patterns similar to Janus simulated structures. The merged information of theoretical simulations and experimental synthesis suggest that Janus structures are the result of a coalescence process between Ag and Cu that fell into a local minima with Janus morphology.

2.2.3 FeNi

FeNi nanoparticle systems are an interesting setup to explore magnetic properties in bimetallic nanoparticle systems, where their magnetic properties are dependent on shape and composition [96, 97]. A recent study already have synthesized these systems with controlled size and composition [97]. At theoretical level, DFT studies have shown that different concentrations favored determined morphologies and atomic distributions [98].

This study over FeNi nanoparticles is used to test the methodology proposed in section 2.1 over bimetallic systems that allows stable alloy motifs at bulk sizes. This system requires a slightly different approach than the one taken in previous section for FeCu and CuAg. In this case, additional structures are generated using alloy bulk lattices along with bcc-Fe and fcc-Ni ones.

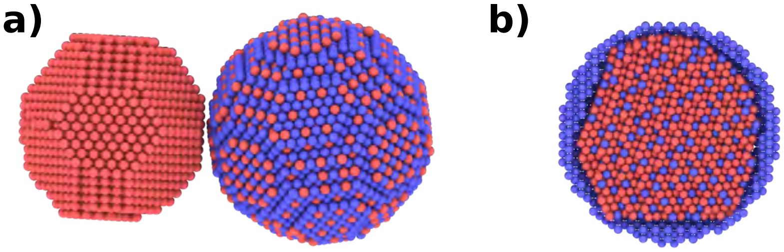

Figure 2.14: Examples of alloy (a) Janus and (b) core-shell initial structures.

Initial alloy settings

Initial systems will be constructed to get an structure with 10000 atoms and 50% Fe concentration. The alloy bulk lattices are generated based on literature bulk phases [99]. These reported lattices bulk phases $FeNi_3$, FeNi and Fe3Ni have a fcc crystal structure. These lattices will not match exactly the number of atoms to get the desired concentration and size. Therefore, a partial alloy spherical cut will be generated limited by the atoms required for each element, in this particular case, to 5000 Ni or Fe atoms. The additional atoms will be added as a single element shell or complementary elemental nanoparticle (see Figure 2.14). These modified initial configurations form an additional set of initial structures that follows the same Janus and core-shell motifs visited in previous sections, but one of their elements is an alloy mix of atoms.

This new set is added to the initial structures pool and then optimized following the same procedure discussed in section 2.1.

Modeling results

The molecular dynamic annealing cycle energies are shown in figure 2.15, which shows a considerable energy difference between completely segregated structures (core-shell

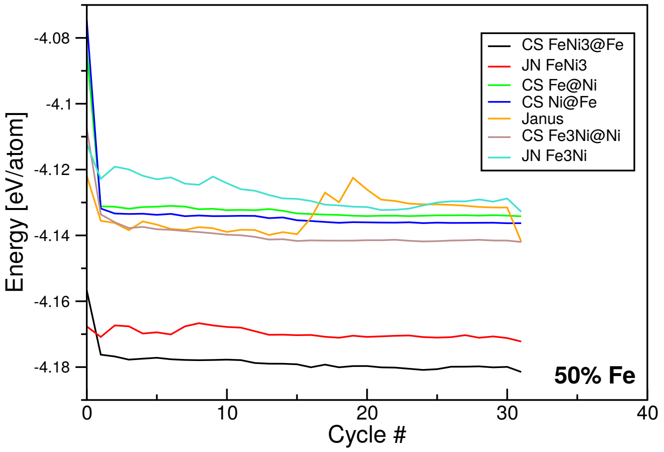

Figure 2.15: Energies from annealing minimization cycles for FeNi

and Janus) and some configurations built with $FeNi_3$ alloy lattices. The alloy structure generated with the FeNi lattice does not appear because it is not stable enough to get into a non-melted minima with a reasonable amount of cycles.

These energy differences are expected because the alloy lattice reduce considerably the energy of non-surface atoms.

In figure 2.16 the three lowest energy configurations are shown. Figures 2.16b/c present a some Ni atoms mixing with the Fe section of the nanoparticle. This behavior is clear evidence of a transitional structure into a lower configuration state. This mixing behavior is not present in Figure 2.16a. There is also evidence of these transitions in the energy cycles, where the search do not show major improvements in energy values.

Discussion

The FeNi results show the importance of including all viable initial configurations to search in the configuration landscape. These results also show that the use of bulk stable states is a key factor to help searching in these nanoparticle sizes, where atomic energy

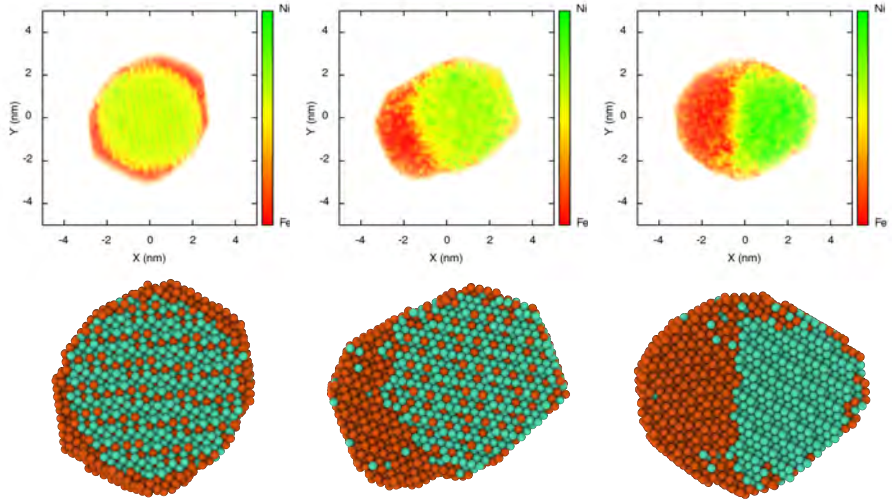

Figure 2.16: (up) Heat map showing Fe (red) Ni (green) elements along with (down) their respective structure cross-sections. The structures presented are the final configurations of (a) CS $FeNi_3$@Fe, (b) Janus $FeNi_3$ and (c) Janus initial configurations.

contributions are more similar to bulk energies and surface energies.

2.3 Neural Networks application: Improving the searching of minimal structures

In some cases the energy calculations for some materials are not described properly by interatomic potentials, such as Au. One of the main distinctively features of Au systems, respect to other metals, is its relativistic effects [100], where an electronic description is necessary to obtain some of the unusual morphologies such as planar or caged/like structures. These morphologies are usually correlated to environmental conditions such as a substrate, temperature, and growing time [101], or related to closed electronic shells of pure and ligand-covering endings of Au clusters [102]. However, if we want to explore local potential minima in the potential energy surface (PES) it becomes a tough problem, because of the number of isomers could increase rapidly with the number N of atoms like exp(N) or even higher. Although, searching for gold global minimum structures has been previously studied following different approaches, these studies have been mainly focused on small clusters [103, 104] or specific atomic numbers [105, 106, 107]. In the case of unsupported clusters, Soler et al. found unusual structures with lower symmetry, for different cluster sizes (38, 55 and 57 atoms), strongly dependent on non-pairwise interactions and its tendency to reduce bonds at the surface, compared to the expected compact ordered geometries[104]. In a similar approach, Deka et al. studied the stability and electronic properties of small $\mathrm{Au_n}$ clusters (n=2-13), following a Density functional theory approach, with BLYP functional and generalized gradient approximation (GGA), and finding minimum energy structures with planar, hollow and compact morphologies[108, 109]. Similar results have been obtained with a classical approach based on a Gupta potential applied to small gold clusters [110], obtaining disordered stable isomers after a genetic-evolutive algorithm is used.

This section is focused on the comparison of minimal structures obtained using interatomic potentials and neural network potentials (NNPs). The work in this section has been made in collaboration with Alexey Kolmogorov, Samad Hajinazar, and Aidan Thorn from Binghamton University, USA.

2.3.1 Methodology

This work requires to train a NNP for Au using DFT energies calculated for a dataset of nanoparticles and bulk structures. The NNP are implemented and trained using MAISE software, which has been used previously in Cu-Ag, Cu-Pt and Ag-Pt systems.[51, 111] The MAISE computational package [51] considers the Behler-Parrinello symmetry functions to replicate the atomic environment for arbitrary bulk systems or nanoparticles. The neural network model was trained using a dataset of 3235 DFT evaluated gold structures of sizes up to 80 atoms, which follows the same procedure used in [51] for single element systems. The train energy error had converged to 9.084 meV/Atom and the test energy error had reached 6.531 meV/Atom.

Evolutionary search

As it was mentioned in chapter 1, the large dimensionality of the surface results in a structurally diverse set of minima so numerous that it proves infeasible to evaluate the energy of each metastable state using density functional theory. Explorations of the PES for the global minima can be performed using an evolutionary search methodology which treats the clusters as population members of a tribe which evolves over a series of generations. At each generation, the structures undergo ionic relaxation using a chosen energy calculation. The fitness function which determines each structure's probability to survive and produce offspring is the model's evaluated energy. The energy calculation also have to reduce its computational cost for these searches because the evaluations must be done over a large number of structutres.

Using a trained neural network as the energy calculation, the search for low energy structures can be accelerated while maintaining an adecuate degree of agreement with DFT. Neural networks are learning machines which excel at interpolation between data points and pattern recognition. Training a neural network model using DFT-evaluated data constructs a PES for the neural network model which closely resembles the DFT PES. Using this NN model, an evolutionary search can be performed to find stable structures at the NN level, which are then relaxed with DFT to reach the minima of the DFT PES.

Multitribe co-evolutionary searches are an extension of the evolutionary search method which evolves a range of sizes in parallel.[51] Existing structures are periodically exchanged between neighboring sizes in the form of "seeds", which allow structural motifs to develop in isolation and then be exchanged with neighbors.

These searches were performed using our NNP and two EAM potentials on gold clusters with a size range of 30 to 80 atoms. The searches had a population of 100 structures, and each exchanged seeds with its neighbors every ten generations. The searches with the classical potentials concluded after 400 generations, but the neural network search was concluded after 250 generations to preserve computational resources, and because the change in energy of the population across generations had become negligible.

The EAM potentials used parameters from the works of Wu et al.[112] and Olsson [113]. The first potential, labeled as "Gupta" potential, is used with a different first neighbor equilibrium distance ($r_{ij}^{(0)} = 2.884$ Å). The second EAM potential is labeled as "EAM".

While the NN and Gupta potentials were implemented into the MAISE software package directly, the EAM interatomic potential was used with the LAMMPS software package [63].

Collection of suitable population members

After the search had concluded for each model, structures from each population were selected for evaluation using DFT. This collection is made to avoid that skip structures with a small energy differences that may be the lower energy structures at DFT level.

For each size of the search, a pool of suitable metastable structures was selected. The criteria for selection of these structures was based on their energy above the ground state of each search and their morphological similarity. The structures are chosen with an energy window above the ground state, where only structures within this window are selected. To avoid duplicates and ensure diversity of structures, a similarity cutoff is used. This is quantified as the dot product of the radial distribution function of each state, which describes the distribution of atoms from the center of the cluster. This implementation ensures rotational invariance, and dot products of the RDF of two structures give an indication of their similarity. For each search, pools were generated using a similarity cutoff of 98% and an energy window large enough to allow many different structures to be chosen. At first, the Gupta, EAM, and NN pools only had five structures, but the NN pool was later expanded to contain 60 structures. All of the structures in the Gupta and EAM pools were relaxed with DFT-PBE, as well as the five state NN pool, but due to the large size of the 60-state NN pool, performing DFT relaxations of each state would prove very time consuming. To preserve computational resources, DFT static calculations were performed on each state of the NN pool, and those structures with an energy within a 10 meV/Atom window of the lowest energy state were selected for further relaxation.

DFT settings

The DFT package used for energy evaluation of the evolutionary search minima was the Vienna Ab-initio Simulation Package (VASP) [114, 115]. The PBE exchange-correlation functional [41, 42] was used with a Projector Augmented Wave pseudopotential [116], as well as a Monkhorst-Pack k-mesh [117] with one k-point at the center of the Brillioun Zone. The relaxation process involved a initial static calculation using an energy cutoff of 500.0 eV for the plane waves, then a relaxation with a lower energy cutoff of 229.948 eV (the default set for the "accurate" option using this parametrization). After relaxation another static calculation was performed with an energy cutoff of 500.0 eV. The reasoning behind this method was to use more accurate calculations at the beginning and end for energy comparisons, and less accurate settings for relaxation to save computational resources.

The simulation box size for all of the clusters was set to 20 Angstroms during relaxation. To test if the interaction between neighboring image clusters would significantly alter energy, structures with image neighbor distances shorter than 7 Angstroms had their box sizes expanded from 20 Angstroms to 25 Angstroms. Static DFT calculations performed on the expanded versions showed that there was no energy difference greater than 0.26 meV/Atom between the expanded and original versions. For the sake of consistency, all static DFT calculations for the final system energies were performed at a 25 Angstrom box size.

Morphology classification

The 60-state NN pool was used to analyze the morphology across all sizes studied. The classification involved a combined use of atomic coordination values, to select specific atoms, and point groups, to determine the symmetry of the selected atoms.

The selection of atoms used the coordination values within a cutoff of 3.2 Angstroms. Three categories were considered to perform symmetry calculations: "high" corresponding to highly coordinated atoms (12), and their first nearest neighbors; "mid" considering all atoms except low coordinated ones (above 7); and "all" where all atoms are included.

Symmetry calculations followed the procedure given by Pilati & Forni and implemented in the SYMMOL computational package [118]. The results will be summarized into 5 symmetry families, without considering the amorphous structures (No symmetry or none), ordered from lowest to highest order: "C" the rotation and reflection family; "D" the dihedral symmetry family; "T" the tetrahedral symmetry family; "O" the octahedral symmetry family; and "I" the icosahedral symmetry family.

The idea of this classification is to find symmetry from the core to the surface of the cluster, avoiding incomplete surface layers.

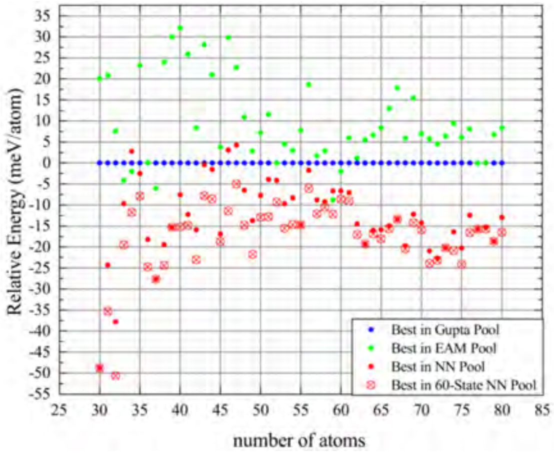

Figure 2.17: Comparison of the DFT-relaxed energies of the minima of the NN model search, the EAM search, and the Gupta model search. Labels under the NN points represent the energy ranking at the neural network level, where one is the ground state.

2.3.2 Results

Search comparisons

Energy comparisons were performed between the most stable state from the NN, Gupta and the EAM 5-state pools. Figure 2.17 shows that the NN search found lower energy structures for almost all sizes when comparing pools of equal size. When using the full 60-state NN pool, the NN search shows lower energy structures for all sizes. However, the ground state at the NN level often did not match with the DFT ground state, often being beyond the first ten members of the pool. This fact forces us to accept that there may be even more stable structures hidden deeper within the population that were simply erroneously classified in energy by the neural network. Extracting these possible structures would require even further expansion of the pool of candidate structures, and greater computational demands due to DFT evaluation of the structures.

It is of significant importance that the NN structures were not only lower in energy, but they also underwent much smaller changes in energy during DFT relaxation compared

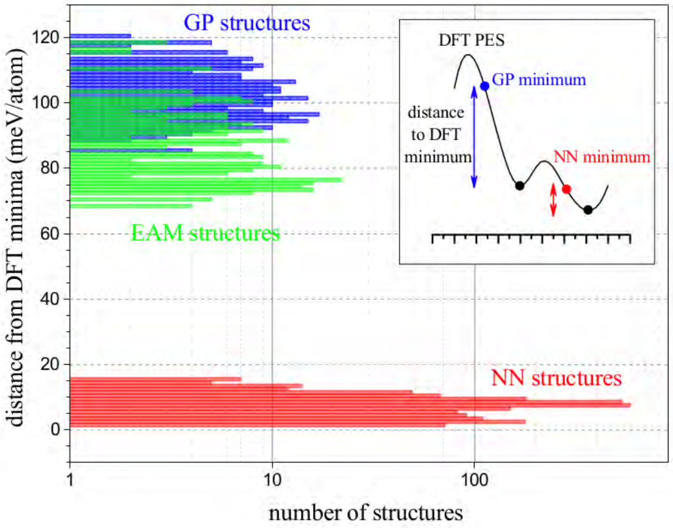

Figure 2.18: Histogram describing DFT energy differences between static and relaxed structures. The structures found using the search with the NN model were generally much closer to DFT PES minima than the structures found with the Gupta potential. The inset plot is a graphical depiction of example states from the Gupta and NN searches on the DFT PES.

to the structures from classical searches, as shown in Figure 2.18. This indicates that the NN structures were much closer to the DFT minima than the classical structures. In addition, the distribution of Gupta and EAM energy change was much larger than the distribution of NN energy changes.

Morphology investigation

Morphology of the different minima states obtained from 60-state NN pool were investigated. These symmetry analisys considered the NN results and their DFT relaxed versions.

The point groups for both versions are presented in Figure 2.19. Each point corresponds to the highest symmetry found among all categories at each structure. The color represents the maximum symmetry found in the structure and the shape shows the

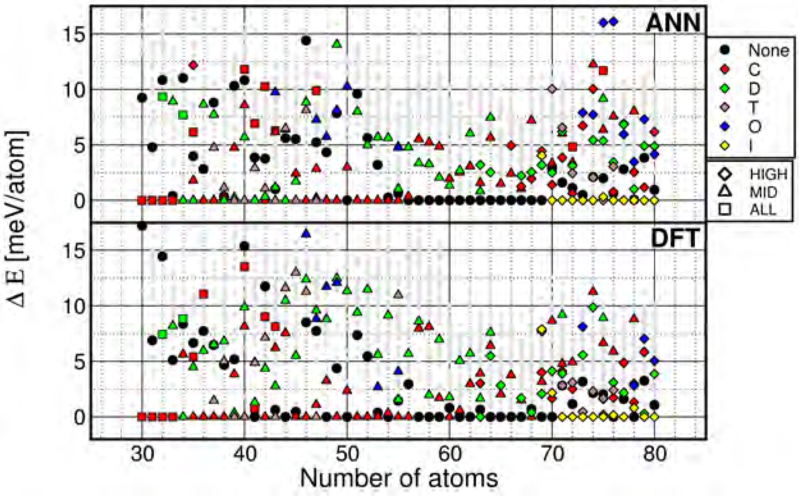

Figure 2.19: Relative energy per atom of gold clusters calculated at ANN and DFT levels as a function of size, with isomers classified according to their point groups.

coordination category where it was found. These points are ploted using their number of atoms and the energy difference from the lowest energy at their respective size.

In general, the optimized candidates and their DFT relaxation show similar features when they are compared at each size, being DFT relaxed energies always lower than ANN results with a mean difference of 7.5 meV/atom.

If we consider the lowest energy at each size, the results show small clusters (30-33 atoms) preferring C symmetries with low coordination, and associated with hollow structures (see Figure 2.20a). From 35 to 56, we have obtained low and mid coordination atoms with zero, C, D and T symmetries, which indicates core atoms effects as the size is increased (see Figure 2.20b). Clusters from 57 to 70 show disordered structures with mainly amorphous (see Figure 2.20c), and few C and D symmetries. Finally, gold clusters between 71 and 80 atoms with high coordination adopted icosahedral symmetry (Ih), corresponding mainly to the core structure (see Figure 2.20d).

For the non-lowest energy structures, amorphous symmetries are still found at all

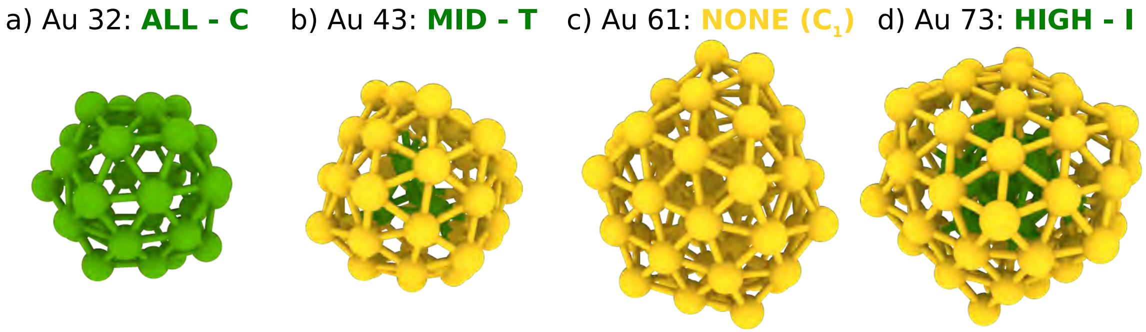

a) Au 32: **ALL - C** b) Au 43: **MID - T** c) Au 61: **NONE (C_1)** d) Au 73: **HIGH - I**

Figure 2.20: Minima energy structures obtained for DFT relaxed 60-state NN pool at different sizes: a) hollow-small 32 atom gold cluster, b) 43 atom cluster with tetrahedric mid-coordinated core, c) an amorphous 61 atom and d) 73 atom with a icosahedral high coordinated core. The green atoms were considered to obtain the calculated symmetry. Amorphous structures do not show green atoms because no symmetry was found.

sizes, while low symmetries (C and D) were classified, respect to size-coordination, as: small-low, medium-mid, and large-high, respectively. T and O symmetries were found for 37-55 (with mid coordination) and from 69-80 cluster sizes (high coordination), and Ih only appeared above 69 atoms. When analyzing the motifs obtained by Schebarchov et al.[119], we can see highly coordinated clusters and symmetries going from C and D at small clusters until D and O groups for large sizes, associated to fcc lattice. These results are clearly different in our case and are mainly a direct consequence of the empirical Gupta potential being unable to consider relativistic effects and therefore to make a correct prediction of stable morphologies. Respect to the comparison for specific and commonly studied cluster sizes, such as 32, 34, 55 and 58. For example for Au32, Johansson predicted I point group [105], while our findings describe a lower C symmetry order. For Au34, Chiriki found a stable configuration with D [120], more symmetric than the D group of our cluster. Additionally, for Au55, Schebarchov and Piotrowski [121] obtained D and disordered core cluster (C), and our predicted minimum has a C point group. Finally, for 58 atoms, Chiriki and Ouyang [106] obtained minima structures with

D symmetries, in contrast to our amorphous minimum cluster.

2.3.3 Discussion

This study shows NN together with an evolutionary searching allows for the exploration of the PES for an entire range of sizes at once, and our NN model is easily transferable to other sizes of clusters of gold, as well as bulk structures. Using a pool of five metastable structures per size for each search, the NN model search found more stable structures compared to the classical potential structures for all sizes except 34, 46, 47, and 59. Using a pool of 60 metastable structures for the NN model allowed it to surpass the other models for all sizes, but it is uncertain whether using the same treatment with the Gupta and EAM searches would allow them to produce more stable structures for some sizes. The search with the Gupta potential produced equivalent or more stable structures than the published structures by Wu et al, which used equivalent Gupta parameters and the dynamic lattice matching method to find stable structures. The structures found with the NN potential were also generally more stable than the structures published by Wales et al. This type of unconstrained search using a neural network model on a large range of cluster sizes is a emerging method, yet we were able to produce competing structures compared to other studies which only investigated specific sizes. An investigation into the hollow cage morphology was performed for small size clusters. It was found that obtained cage structures for size 30-33 were stable at the DFT level, while the classical potentials only had solid structures in their morphology.

Chapter 3

Mechanical and structural properties in one-dimensional nanostructures

In one-dimensional structures, contrary to nanoparticles, there are only two dimensions constrained to the nanoscale, because now exists periodicity in one dimension. These structures present a more different shape than a sphere, compared with nanoparticles, which implies that they are meta-stable structures, according to the simple energy model presented in chapter one. Theoretical modeling in these structures considers initial cylindrical structures, instead of spherical, to impose periodicity in one dimension. Additionally, the local search in the PES is simplified using a structural thermalization, since the desired structure is previously provided. In this chapter, motivated by the evidence of synthesized polycrystalline Ni nanotubes, we study, using molecular dynamics simulations, the mechanical properties of bimetallic FeNi nanowires during the uniaxial tensile and compressive deformation. In order to compare the combined effect of both metals, we first study the stress-strain curve, grain boundary rotation, planar defect populations and the fracture mechanism of isolated nanowire and nanotube systems under tension and compression, with the same lengths and diameters.

3.1 Metallic nanotubes/nanowires under mechanical deformation

Nanomaterials such as nanotubes (NT), nanowires (NW) and pillars with different crystallinity are very promising structures, due to their combined mechanical and electronic properties, even under axial tensile stress [122]. In particular, considerable attention is focused on nanotubes because of their two easy-to-modify surfaces and a lesser weight than nanowires, making them attractive candidates to build reliable electromechanical devices and less prone to sedimentation for biological applications or ferrofluids [123]. In this context, there are several theoretical and experimental reports referring to the mechanical response of monocrystalline nanowires and nanotubes, obtaining in general, a sharp fall in the stress-strain curve reported in the plastic deformation zone based on the nucleation of alternating dislocations [124, 125, 126, 127, 128]. In particular, Huang et al. studied the tensile strain effect on fcc nickel nanowires, finding a stress-strain response with identical trend respect to polycrystalline metals [129]. Also, mechanical properties of metallic tubes have been studied both theoretical and experimentally, for example, Seo et al. considered the grain size effect on the flow stress of hollow Ni pillars [130], while Xu et al. studied the asymmetry of tensile-compressive loading of tungsten nanotubes, as well as the different regimes of thin and thick walls [131]. Also, Wang et al. observed significant nucleation of dislocations for twinned Ni NW under bending [132], while Cao et al. detected partial dislocations in Au nanotubes with thin walls (1 or 2 nm) [126]. Nanowires and nanotubes can be synthesized by several techniques such as electrospinning, electrochemical deposition, chemical vapor deposition, and atomic layer deposition, among others [133, 134, 135, 123]. In particular, the nanotubes synthesized by electrodeposition techniques are not pure crystalline structures but contain grains [136], that could affect their mechanical properties such as Young's modulus or the plastic zone regimes, where a non-abrupt fall in the stress-strain curve is observed for nanowires [137]. Besides, different kinds of planar defects, such as stacking faults (SF) and twins, could be obtained by the grain boundaries (GB) [138, 139, 140], moving through the grains and interacting among them, affecting the fracture mechanism of the nanotubes under applied stress.

3.1.1 Methodology

A detailed study of a polycrystalline NT was made using atomistic simulations, which is supported by the experimental evidence and synthesis protocols presented in this work. Here, it is important to mention that the experimental diameters are in general larger than those considered in our simulations. However, we expect that our results presented here could be extrapolated without loss of generality, as far as the NT and NW comparison is concerned.

Computational Method

Atomistic simulations of polycrystalline Ni nanotubes under uniaxial tensile load have been studied by means of molecular dynamics simulations using the LAMMPS code.[141] The interaction between Ni atoms was modeled using an embedded atom method (EAM) potential,[142] with a parameterization given by Mishin et al.[143] Extensive validation of the mechanical properties using this potential has been already reported for metals such as Cu and Ni.[144, 145, 146, 147, 148] The simulated nanotube was built from a nanocrystalline Ni bulk sample with a mean grain size of 5 nm, where its nanocrystalline structure was created by means of a Voronoi Tessellation algorithm, and then relaxed with the same procedure reported for other nanocrystalline materials, such as, Cu,[139] Fe,[149] and diamond.[150, 151] From this relaxed structure, a nanotube was created by cutting two concentric cylinders with internal and external radii given in the nanocrystalline sample, obtaining nanotubes with different thicknesses. In order to diminish the boundary effect, three different axial lengths were considered, defining a form factor (FF) as the ratio between the axial length and the diameter of the nanostructure. Due to the artificial cut used in the construction of the nanotube, remnant stress produced by the surface cut or cavity presence is expected. Therefore, the potential energy and stress of the nanotube were reduced in a two steps process: First, a conjugate gradient optimization, allowing a box-size adjustment is used to relieve stress and reduce energy. Then, to allow surface reconstruction and grain boundary accommodation, a relaxation at 300 K using a velocity rescale algorithm coupling with a zero pressure barostat in z-axis during 100 ps was performed. In this way, we obtain nanotubes with an axial pressure component lower than 10-5 GPa. The uniaxial tensile loading was performed along the z-axis with a strain rate of 108 s-1. During the load, NT temperature is held at 300 K using a velocity rescale algorithm with a timestep of 1.0 fs.

Defects and dislocations analysis were carried out by using a common neighbor analysis (CNA) and DXA algorithm,[152] both methods implemented in OVITO software.[153] Stress values were computed by LAMMPS, considering a volume correction calculated by OVITO construct surface mesh calculation. A more accurate defect classification was obtained with the Crystallographic Analysis Tool (CAT) code, [152] and the local crystallographic orientation (LCO) method.[154] These codes are prepared by a set of algorithms which, through a previously established pattern database, allows the identification of planar defects such as, stacking faults or twin boundaries, and grain orientation analysis of polycrystals, among others.

Experimental evidence

To support the fact that nanotubes and nanowires can become polycrystalline, Ni nanotubes within the pores of a porous alumina membrane by the atomic layer deposition

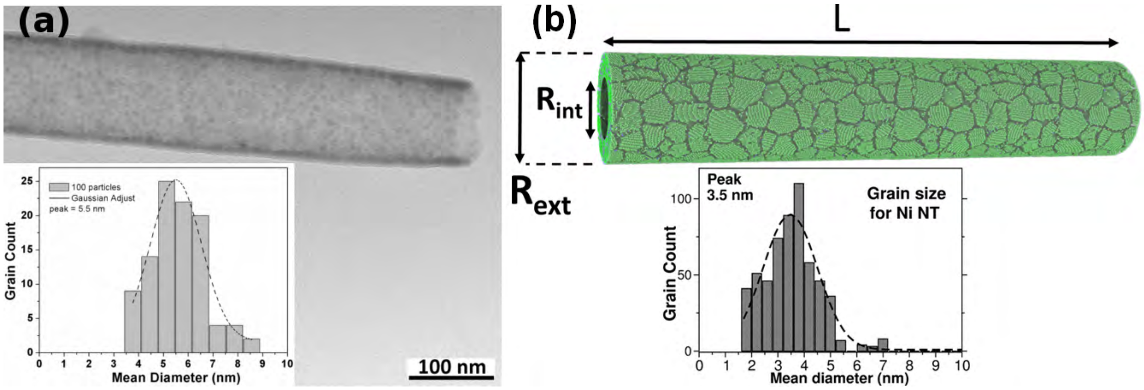

Figure 3.1: (a) TEM image of a freestanding Ni nanotube released from AAO template with a wall thickness of about 14 nm. (b) Modeled polycrystalline Ni nanotube and size distribution for Ni grains. Experimental images obtaines in collaboration with Juan Escrig, Juan Luis Palma and Alejandro Pereira

(ALD) technique [134] has been synthesized with an anodization process. The synthesis of Ni nanotubes is possible thank to the collaboration with Juan Escrig, Juan Luis Palman and Alejando Pereira. From the synthesis, NiO nanotubes are transformed into Ni nanotubes following a thermal reduction process. Finally, scanning electron microscopy (SEM) and transmission electron microscopy were carried out to investigate the morphology of nanotubes.

3.1.2 Mechanical deformation of Ni NT and NW under tensile strain

The mechanical properties of Ni nanotubes were evaluated and compared with Ni nanowires. Experimental evidence of polycrystalline nanotube is also shown identifying similar features compared to the modeled structures.

The morphological characterization of an experimentally synthesized and isolated nanotube is shown in Figure 3.1a. We can see the morphology of the polycrystalline nanotube, constituted by grains with an average diameter size of 5.5 nm. In order to

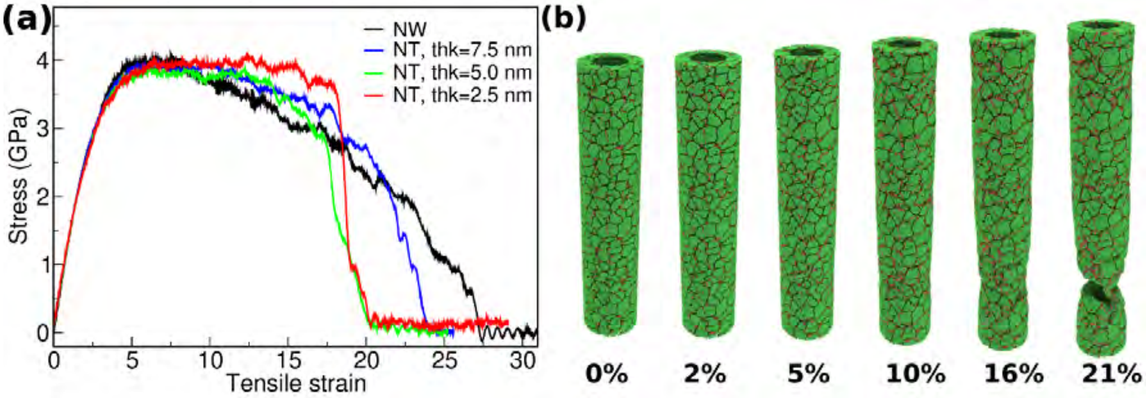

Figure 3.2: (a) Stress-strain curves for Ni polycrystalline NT and NW at different thickness. (b) Polycrystalline Ni NT with FF 4.8 under different applied strain, showing the FCC (green) and HCP (red) detected atoms by common neighbor analysis.

simulate and evaluate the mechanical properties of Ni nanotubes, we have considered polycrystalline nickel nanotubes as depicted in Figure 3.1b, with an average grain size of 3.5 nm, smaller than the experimental evidence. This feature is attributed to the modeling setup, where an original cubic periodic system containing grains with 5 nm size was used to carve a nanotube with an outer radius of 11 nm and three possible inner radii of 3.5, 5 and 8.5 nm, respectively, and promoting the formation of smaller grains. Grain boundaries in modeled NT are not shown in the relaxed structure (Figure 3.1b) for better identification of grains.

Once the nanotube is prepared, we applied a uniaxial tensile loading to obtain the stress-strain behavior for polycrystalline Ni nanotubes. The results obtained with FF 1.6, 4.8 and 6.4 revealed a fracture point at a tensile strain of 60, 21 and 19 respectively, being the first one mainly attributed to finite size effects. From these results we have chosen to continue our simulation with a FF of 4.8 for the rest of the study, avoiding periodic boundary effects (FF 1.6) and larger systems with higher computational cost (FF 6.4). Figure 3.2a shows the stress-strain curves comparing the NW (black line) and

NTs response with different thickness (thk): 2.5 (green), 5 (red) and 7.5 nm (blue), corresponding to a 40.3%, 70.2% and 89.9% of the NW volumetric mass respectively. Additionally, Figure 3.2b shows the common neighbor analysis (CNA) of NT with thk=5 nm, depicting FCC (green) and HCP (red) atoms. We observe that NW and NT behave very similar in the elastic zone, with Young's modulus between 140 GPa and 142 GPa, for NW and NT, respectively while the yield strength is the same for all cases. Different mechanical behavior is observed in at larger strains, finding a fracture point at a tensile strain of 21, 21, 23 and 27% for thickness values of 2.5, 5, 7.5 and 11 nm respectively. We must emphasize that in our simulations, despite the NW including GBs, we do not observe a completely brittle fracture due to GB decohesion, but also a ductile fracture promoted by grain GB sliding and necking, as seen in the Figure 3.2b. This fracture process is somewhat unlike to what was reported by Srolovitz and coworkers for nanocrystalline Ni wires, where a ductile to brittle transition is expected for a nanowire with a larger aspect ratio compared to our case.[137]

In order to obtain a better understanding of the deformation under strain in polycrystalline Ni nanotubes, we have calculated the atomic displacement at different strains for this nanostructure using OVITO's displacement modifier. Here, before the displacements, an affine mapping of the reference set, respect to the current simulation box of NT with thk of 5nm (see Figure 3.3a) is performed. Here the greatest magnitude of displacement, with respect to the initial positions, is located around the fracture zone. In addition, the applied strain promotes grain boundary activity ranging from a general displacement at 5 %, shown as a clear peak in Figure 3.3a, to the formation of two and more displacement peaks at 16 and 21 %, being these groups shown in blue, green and red related to small, medium and large changes respectively. This information is emphasized in Figure 3.3b, where the atomic displacement is depicted at different strain intensities. The higher

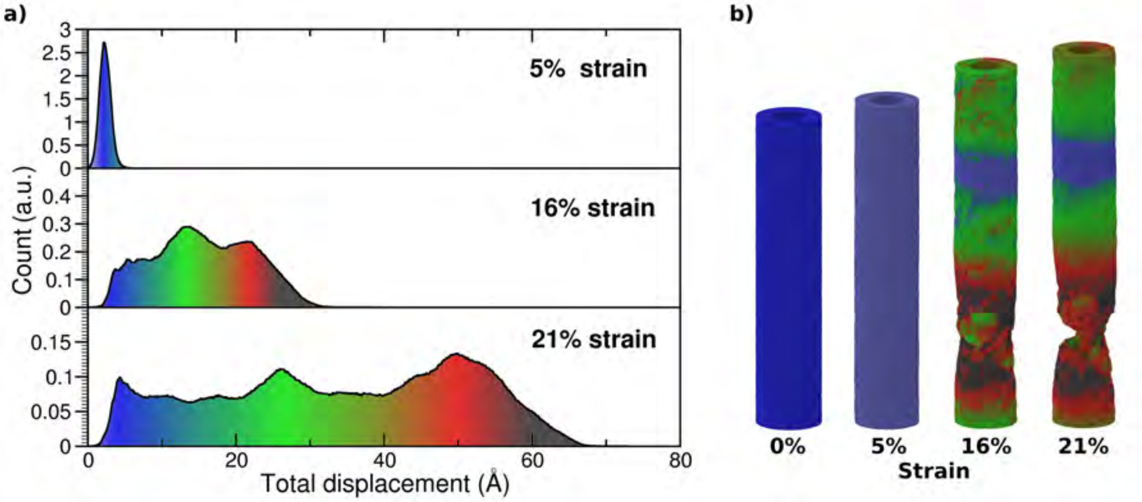

Figure 3.3: Displacement analysis of a NT with a thk=5nm. Blue, green and red colors represent small, medium and large displacements respectively.

displacement is located around the breaking zone and clearly seen at 16 % and 21 %. We also calculated the radial displacement, finding one clear peak shifted up to 0.3 nm in the radial direction, with the same behavior for NT and NW. Finally, both the inner and outer radii of the nanotube are reduced during the tensile strain, which is confirmed by the necking effect observed around the fracture region, while for the NW a slightly reduced diameter is obtained up to the breaking point.

Figure 3.4 shows the local grain orientation for thin NT (thk=5nm) and NW, obtained from atomistic analysis of crystal structure and defects.[154] Here the crystallographic orientations of each grain (in this case a FCC lattice) are defined as red [001], green [011] and blue [111]. The transition of NT from 5% to 16% shows localized grain coarsening together with partial grain rotation (see labeled grains 1, 2 and 3 in Figure 3.4). Further grain rotation in NT leads to intergranular fracture at a high-angle grain boundary (16%), which grows thanks to additional grain rotation (21% and 23%).

Most of the nanotube grains remain with the same orientation, at both sides of

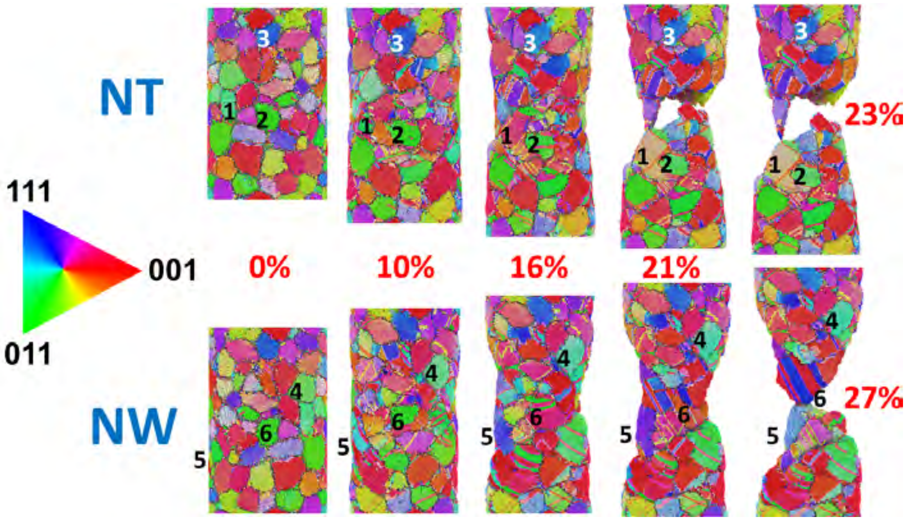

Figure 3.4: Local crystallographic orientation of the grains in a NW and a NT with thk=5nm at different percentages of strain. Grains are depicted and colored to visualize crystallographic orientation in FCC lattice (red=[001], green=[011], blue=[111]). The highest strain for NT and NW is 23 % and 27 %, respectively.

the fracture region. In contrast, the NW transition shows a dominance of the plastic necking of grains (from 16 % to 27 %), similar to the results reported by Wu et al.[137] Additionally, labeled grains 4, 5 and 6 show a clear rotation of the polycrystalline NW during necking phase.

3.1.3 Dislocation analysis

In order to understand the mechanisms involved in the plastic regime and the fracture of thin NT, we study the population of defects present in NT and NW as a function of the deformation. It should be noticed, that a considerable fraction of SF and twin boundaries are created after the sample relaxation. The ultra-small grain size and large GB area allow the nucleation of hcp planes in many grains.

The nucleation and growth of planar defects are illustrated in Figure 3.5a depicting the local change of planar defects as a function of strain, and relative to the NT with 0

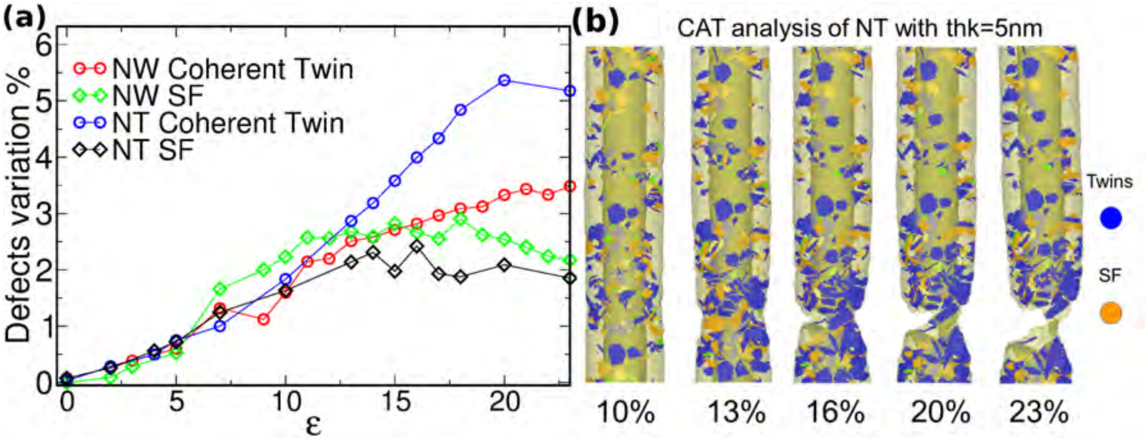

Figure 3.5: (a) Planar defects analysis for thin NT and NW. Counts were considered in a specific zone of 30 nm around the fracture region. (b) CAT of NT with thk=5nm depicting the most relevant planar defects in the NT at different strains. Transparent region delimits the NT inner and outer radii, while the colors depict twins (blue), simple stacking faults (orange). FCC and grain boundary atoms were removed for a better description.

% of strain. In particular, this graph shows that although the SF formation is observed for both geometries, the increase, at high strains, of twin boundary percentage of the NT is remarkably higher than in NW. In Figure 3.5b, planar defects for different strain rates are displayed observing that even at small strains exist evidence of glide planes, a condition that in the crystalline counterpart determine the onset of plasticity. However, in polycrystalline NT and NW, the largest partial dislocation emitted is confined by the grains and/or the NT wall thickness so that any of these plastic events are negligible at lower strain rates. Figure 3.5a shows that the onset of SF and twin generation occurs even at very low strains. For grains below 5nm, GB activity is expected to dominate over dislocation-based plasticity.[155] Due to the small grain size, leading partial dislocations are emitted and propagated throughout the entire grain, without emission of a trailing dislocation which would generate a full dislocation. Partial dislocations emitted in three consecutive planes would lead to nanotwins. Figure 3.5a shows that the stacking fault and twin boundaries are emitted by equal at strains below 10 %. This behavior is contrary to the observed in single crystals or NC materials of larger grains, where SF are predominant near to yield point. However, if the strain increase, the twin boundary formation is predominant over any other defective structure with a maximum relative value of 5.5 % and remains constant even during the NT failure. On the other hand, the SFs decrease in number once the NT fracture starts, due to their absorption with the free surface and the stress relaxation, giving some signals that fracture mechanism is twin boundary assisted. Here there is a clear accumulation of defective atoms in the necking region neighborhood, in agreement with displacement localization discussed previously. Additionally, a local defects count (30nm around the fracture) reveals that between all of them, a 54% corresponds to twin boundaries. Based on these results, we expected that NT failure is a twin assisted process.

3.1.4 Mechanical response of Ni NT and NW under compression strain

The development of lightweight hierarchically metallic nanostructures is an alternative to obtain novel and unexpected mechanical properties that have been extensively studied in the last years.[156, 157] Usually, the structure corresponds to a collection of nanotubes or nanowires, mainly nanocrystalline, self-assembled as building blocks and displayed in a suitable arrangement that ensures a cooperative response of all its constituents at a given deformation.[158, 159, 160, 161] Thus, the expressed mechanical properties are dependent on the nanostructure design, and of the mechanical properties of the nano-object used for its building.[162] Even though the study of mechanical properties of metallic c- and nc-NW counts with extensive research among years,[129, 163, 164, 165, 166] unfortunately not same attention has been put in the hollow counterpart, probably due to lack of experiments in the matter. Nowadays, the development of atomic layer deposition technique allows the successful synthesis of nc-NT with an adjustable combination of geometrical parameters,[134] and nanocrystalline texture close to the 5nm of grain size. It is worth to notice, that NT is a lightweight version of NW with a higher surface to volume ratio and lower specific density, features that made them excellent candidates for catalysis, energy devices and design of novel nanostructures.[167] The use of NT and NW for nanostructured devices implies to understand how the filaments will respond under tensile and compressive deformation. In the previous section the study of Ni nc-NT under tension revealed that nanotubes with a mass reduction close to the 60% behave similar than nc-NW in the elastic regime and yield strength, with a small difference in the fracture point. In compression, finite elements models highlighted buckling in thin-walled nanotubes, but the model does not predict complex defects as dislocations or grain boundary structure.[168] Molecular dynamics simulations show that crystalline NW allow stacking faults and twins driven by surface tensile stress, assisted by partials dislocations.[163] Monk and Farkas [169] show the asymmetric behavior under tension-compression of nc-NW with 10nm grain size, they conclude that plasticity in NW with a relatively small diameter is mediated by grain boundary slide over the dislocation activity. Modeling nc-NW and NTs under experimental conditions implies the inclusion of ultra-small grain size, where grain boundary activity could be predominant. Additionally, the high specific surface areas of NT design allows a much rich behavior for grain displacement and dislocations movement. All in all, in this work we report by means of molecular dynamics simulations, the combined effect of mechanical compression on polycrystalline NT and NW with ultrafine Ni grains. We addressed the mechanism followed during the plastic regime at high compressive deformation, and compare the difference between nc-NT and nc-NW with the pristine counterparts.

Methodology

Uniaxial compressive strain is addressed using molecular dynamics simulations employing the LAMMPS code [141]. Ni atoms interaction is modeled with the embedded atom method potential,[142] with the parametrization proposed by Mishin et al.,[143] that reproduce several physical quantities such as elastic constants,[170] stacking faults energy,[171] among others.[172] The nanocrystalline structure was given by cutting NWs and NTs from a Ni nc-bulk sample with 5nm mean grain size. Nc bulk with an expected grain size was built employing a Voronoi tessellation algorithm, where this grain size distribution can be achieved in experiments utilizing atomic layer deposition techniques.[134] Usually, Voronoi constructions give grain boundary structures far from equilibrium; therefore, high energy grain boundaries have to be relaxed to avoid any possible artifact at the moment to characterize the material mechanical properties. The nc bulk sample was prepared by removing overlapping of nc bulk, and then the grain boundary structure was relaxed by means of a zero pressure barostat coupled with a 300 K thermostat, following the procedure presented by Bringa et al.,[173] further details of this procedure can be found elsewhere.[150, 151] The NW and NT with the desired radius and thickness are carved from the nc template and relaxed again with a velocity rescale algorithm at 300K during 100 ps coupled with a zero pressure barostat in the cylinder axial direction.

3.1.5 Mechanical response under Loading/unloading processes

Uniaxial compression was carried out along the z-axis with a strain rate of 108s-1 and a timestep of 1.0 fs. The system temperature was held at 300 K during the simulations. Each nanostructure is then compressed a 30% of its initial length, and defects detection and visualization were carried out with OVITO code,[153] while dislocations and planar defect identification were performed with the Dislocation extraction algorithm[153] and

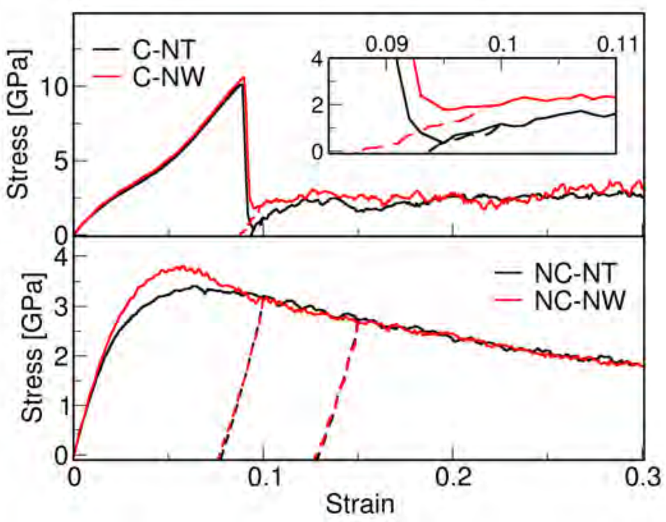

Figure 3.6: Compression Stress-strain curves for Ni crystalline (upside) and nanocrystalline (downside) NT and NW. Unloading process are depicted from strain 0.1 and 0.15 respectively.

the Crystal analysis Tool.[152] The characterization of the simulated nanotubes and nanowires is performed by common neighbor analysis (CNA) and DXA algorithm, being both tools included in OVITO package to study defects and dislocations.

A uniaxial compression is applied until a strain of 0.3, respect to the initial length is considered, and the stress-strain result is shown in Fig.3.6. Here we can see the behavior of crystalline NT and NW (Fig. 3.6a), with a characteristic elastic regime with a monotonic increase going from 0 to 0.9 of applied strain. At this point, we observe a significant drop in the stress, where the NT has the largest drop (97% compared to 84% of NW).

In Figure 3.7 we show snapshots from the compression of crystalline NT and NW. Although both fail brittle around a 0.09 strain, the response just after both reaches the ultimate strength is different. As mentioned before, the stress drop for NT is bigger than for the NW. For the case of NT it is quite apparent that the failure is more localized than

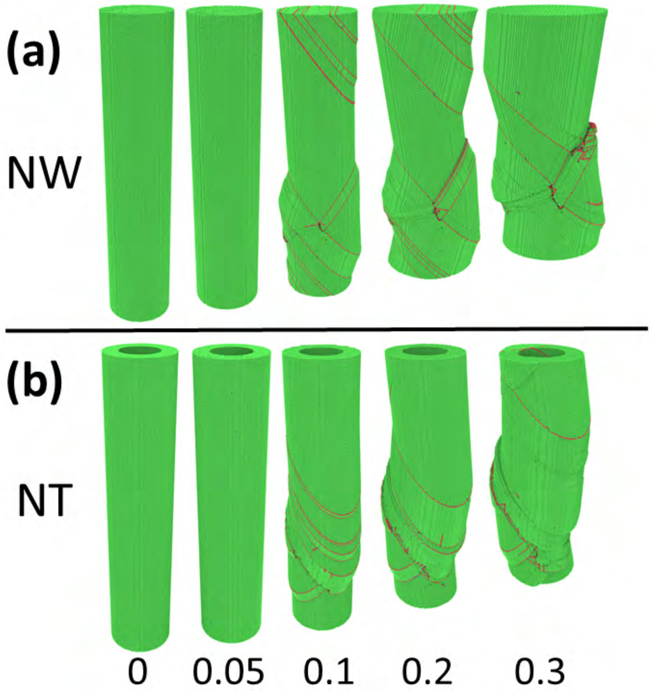

Figure 3.7: Snapshots of crystalline (a) NW and (b) NT under different applied compression strains, showing the FCC (green), BCC (blue) and HCP (red) detected atoms by common neighbor analysis (CNA).

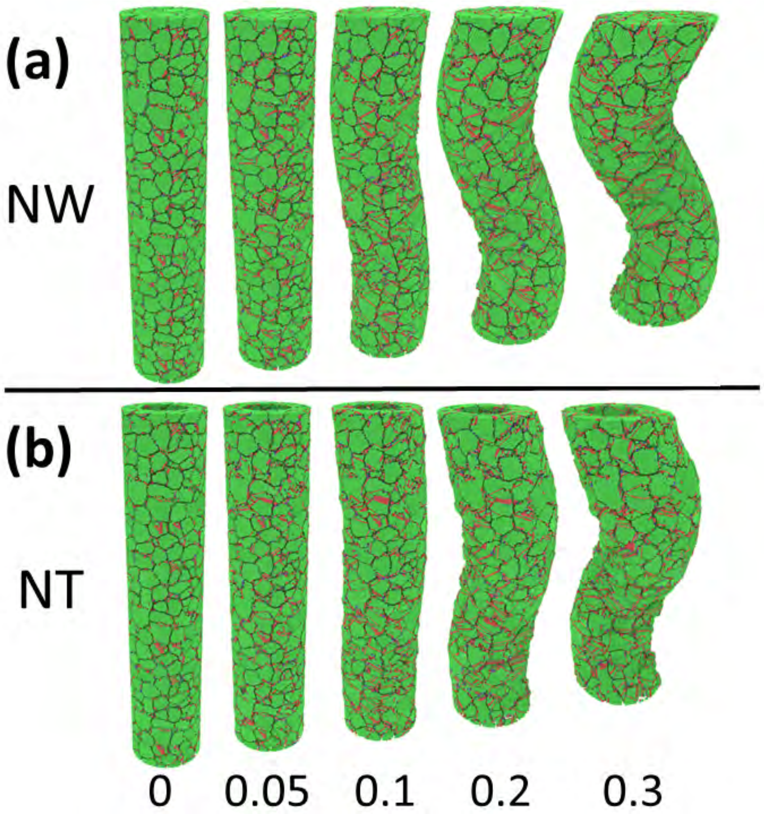

Figure 3.8: Snapshots of nanocrystalline (a) NW and (b) NT under different applied compression strains, depicting the FCC (green), BCC (blue) and HCP (red) detected atoms by common neighbor analysis (CNA).

in the NW case, a situation that can be observed for a strain of 0.1 and 0.2. In Figure 3.8 we show the compression of nanocrystalline NT and NW. Opposed to the crystalline cases, the compression response of nanocrystalline NT and NW is quite similar. The principal difference observed is that the NT reaches a slightly higher ultimate strength at strain 0.05. Additionally, Figure 3.8 shows that both NT and NW coil under compression.

We have also studied these systems when the applied load is removed at a strain of 0.1 and 0.15 respectively. Inset in Figure 3.6 illustrates the strain-stress curves (segmented lines) when the crystalline systems are unloading. From this figure we can see that 0.1

corresponds to a strain after the ultimate stress for our system is reached. We observe that the crystalline nanotube and nanowire (Figure 3.6a) have a higher residual strain than the nanocrystalline nanotube and nanowire (Figure 3.6b), i.e., the nanocrystalline nanotube and nanowire have a best partially elastic behavior than the crystalline nanowire and nanotube. For crystalline nanotubes and nanowires at a strain of 0.1 (see Figure 3.6), we observe planes where the atoms are organized like hcp with twin boundary defects. The creation of these planes prevents bending of these systems. Therefore, the elastic recovery zone is very small when the crystalline nanowire and nanotubes are unloaded. However, for nanocrystalline nanotubes and nanowires at a strain of 0.1, there are grain boundaries where the atoms are forming like hcp with stacking faults and twin boundary defects. When the systems have this strain, the grain boundaries form a bent nanowire or nanotube when these grains were reorganized. Then, the crystalline nanotubes and nanowires have a region where these systems could be partially unbending, i.e., the residual strain for the nanocrystalline nanotube and nanowire is less than the residual strain for the crystalline nanotube and nanowire.

3.1.6 Dislocation analysis

From figure 3.9 crystalline and nc structure show a high difference in planar defects formations. In c-NT and c-NW a compressive strain of 0.7 is required for nucleation of first planar defects, in both cases is observed that the plasticity onset is assisted by twinning along the preferential 111 planes. In nc systems, SF and twins are observed at zero strain, due that the ultrasmall grain size allows the nucleation of faults during the nc relaxation. Significant difference rise with crystalline cases, where NT and NW seem to be prone to produce more planar defects as strain gets higher. Additionally, nc-NT and nc-NW geometry show the same behavior from small strain and until a strain close to 0.3 is reached, so we conclude that formation of planar defects is dominated

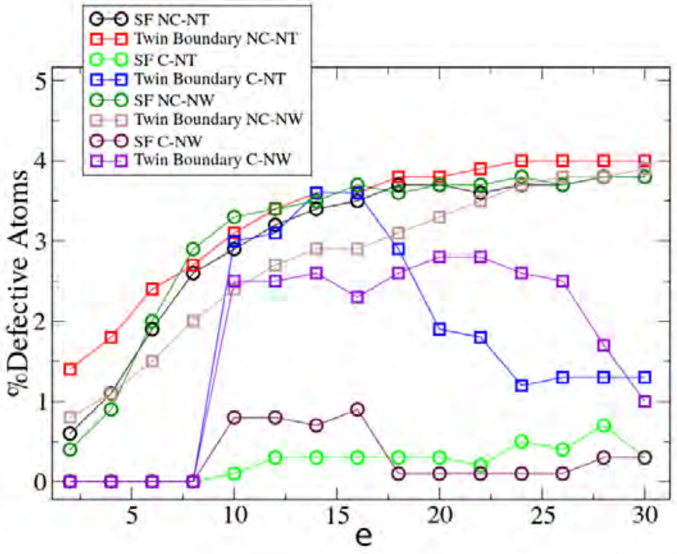

Figure 3.9: (a) Planar defects analysis for NT and NW. Counts were considered in a specific zone of XX nm around the fracture region. (b) CAT of NW with thk=5nm depicting the most relevant planar defects in the NW at different strains.

by the grain boundary structure and not with the tubular or wire design. In contrast to the nc-NT under tension, a twin dominant fracture is obtained, in compression a different deformation mechanics is observed at least for nc systems where coiling can avoid localizations of larger stress concentrations. While in the crystalline systems, the absence of grain boundary favors detwinning and SF fault absorption on free surfaces at higher compressions.

It is straightforward that nc-NT and nc-NW softening is attributed to the inverse Hall-Petch since the grain size does not surpass the 5nm. From Figure 3.10, it is shown that dislocations are observed at strains lower than 0.2, the high surface stress of the small grain size allows the formation of partial dislocations at very small loads, however, plastic activity is not expressed in the strain-stress curves since the larger dislocations line nucleated cannot surpass the larger grain size. Such small size avoids dislocation pileup

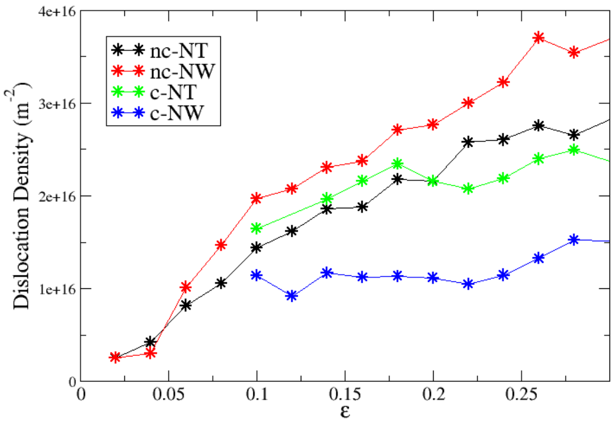

Figure 3.10: (a) Dislocation density in Ni NT and NW.

and hardening, in fact, a dynamical behavior of dislocation absorption and production is observed in the grain boundary structure. The dislocations dynamics, in addition to the grain boundary sliding, are not only responsible of NT and NW softening but also of the rich and smooth behavior of the stress-strain curve beyond the elastic limit. It worth to notice, that dislocations density is not zero at e=0.1 while the elastic limit is registered at lower deformations, the discrepancy attributed to the formation of partial dislocations are rapidly absorbed by the opposite surface, leading only planar defects as trace.

3.1.7 Summary and conclusions

A theoretical study of the mechanical response of polycrystalline NT and NW has been performed through elastic and plastic regimes. The modeled NT structure is similar to the synthesized NT with polycrystalline morphology. We have obtained stacking faults and twin boundaries emitted by equal at low tensile strains. The stress-strain curve reveals that NT and NW have a close behavior under moderated uniaxial deformation,

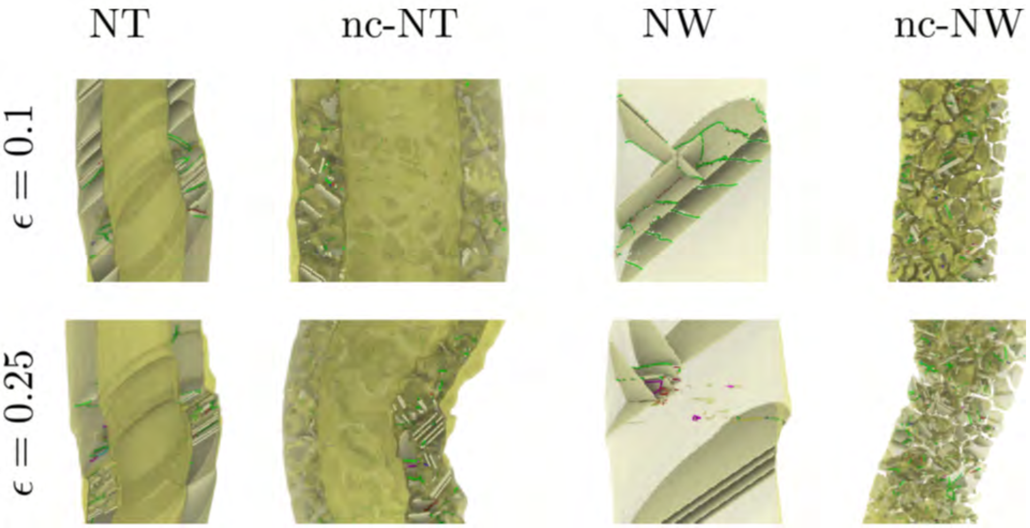

Figure 3.11: Stacking faults and twinnings

with similar Young modulus and critical stress. However, if the strain is increased, a twin boundary formation starts to be significant showing evidence of a fracture mechanism as a twin boundary assisted process. Here the coherent twins formation is higher in thin NTs than with NW, around the fracture zone. This difference is directly related to a lower strain required to fracture the NTs than NW. Additionally, the fracture is due to the defective atoms accumulated in the necking region shown by the atomic displacement curve under deformation. Also, the NTs studied here with a lesser volumetric mass of 90, 70 and 40 % could be envisaged as the ultimate lighter material compared to NWs. In the case of compressive strain applied to NT and NW, a clear difference is observed between crystalline and nanocrystalline materials, being the first dominated by the formation of large planar defects, while the nc-NT and nc-NW show a coiling structure, avoiding large stress regions. Future work is addressed to analyze the response under compression where the cavity of the NT might lead to larger tension/compression asymmetry. Larger grain sizes might also display different fracture mechanism, with contributions from full dislocations.

3.2 Bimetallic nanowires under tension and compression

The study of bimetallic nanowires offers the possibility to design new nanoelectronic devices [174], where the strength of the combined materials strongly depends on the interface between both components. In this context, deformation of Au/Ag crystalline nanowires have been studied obtaining similar Young Moduli for both compression and tension [175]. In this section, we report the combined effect of polycrystalline Fe and Ni grains on the mechanical response of bimetallic nanowires by using theoretical modeling. By means of classical molecular dynamics simulations, we study the breaking process mediated by atomic dislocations, following the stress-strain response under tension and compression regimes. Structural and composition analysis was performed during the deformation.

3.2.1 Methodology

A classical molecular dynamics approach was used to model the breaking process of mono and binary metallic NWs. The theoretical procedure of this study is rather similar to the previous ones developed for monometallic Ni NT and NW. These simulations were performed with LAMMPS code,[141] and modeled with the embedded atom method parameterized by Bonny et al. for Fe-Ni systems.[176] In this case the average grain size is adjusted to 3.5 nm after carving the structure to obtain a NW of Fe and Ni with a diameter of 22 nm for both cases. Following the same procedure as before we have studied the tensile strain effect on both nanowires depicting different configurations in Fig 3.12, from 0 strain until the rupture point.

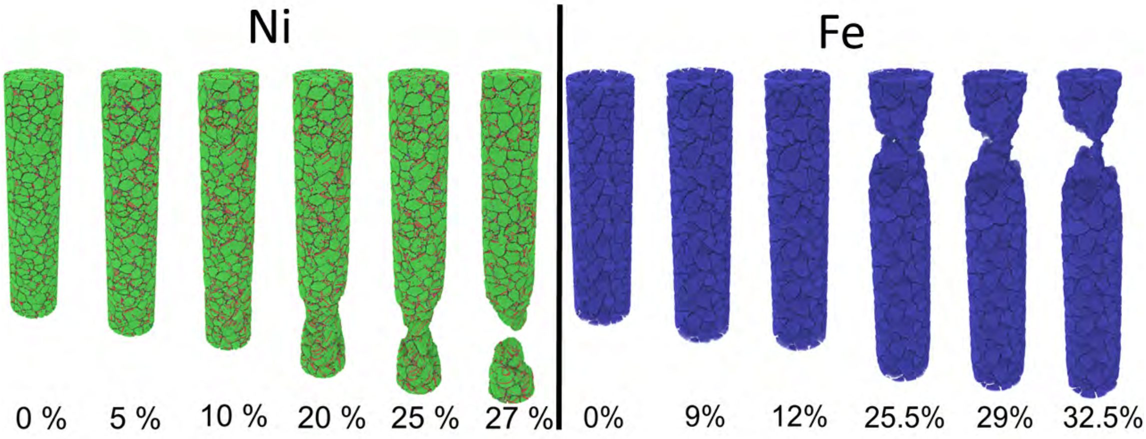

Figure 3.12: Snapshots of polycrystalline Ni and Fe NW under different applied tensile strain. FCC (green), BCC (blue) atoms and HCP (red) are depicted for better comparison.

3.2.2 Mechanical response of mono and bimetallic nanowires

Once we have obtained the mechanical response of the monoatomic wires, we prepared the bimetallic nanowire considering a Fe core/Ni shell structure with an inner and outer diameter of 11 nm and 22 nm respectively. Figure 3.13 shows the deformation of the bimetallic system at different percentage strain respect to the initial configuration. Both results show a plastic zone following a ductile fracture, especially for Ni and FeNi system.

The stress-strain curves are shown in Figure 3.14, where we can see the behavior of monoatomic and bimetallic systems. In particular, it is interesting to see the rupture point for all cases, where Ni NW has the lowest strain at 0.27, followed by Fe NW at 0.33, and finally FeNi NW at 0.4 strain. The last results suggests a more ductile breaking process of the structure during the plastic zone, surpassing the response of the monoatomic systems. Also, it is noteworthy to see the diminished stress in the bimetallic system, compared to the previous cases.

We have also considered the mechanical response under compressive deformation, for

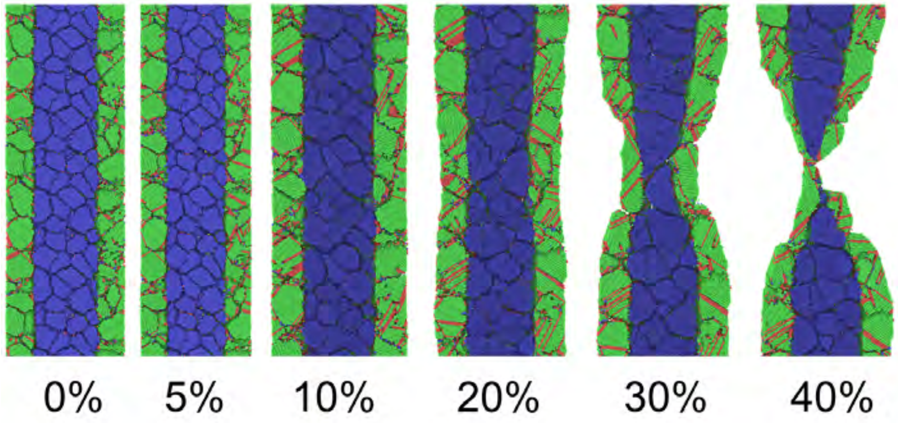

Figure 3.13: Snapshots of polycrystalline NiFe NW under different applied tensile strains, showing the FCC (green), BCC (blue) and HCP (red) detected atoms by common neighbor analysis (CNA).

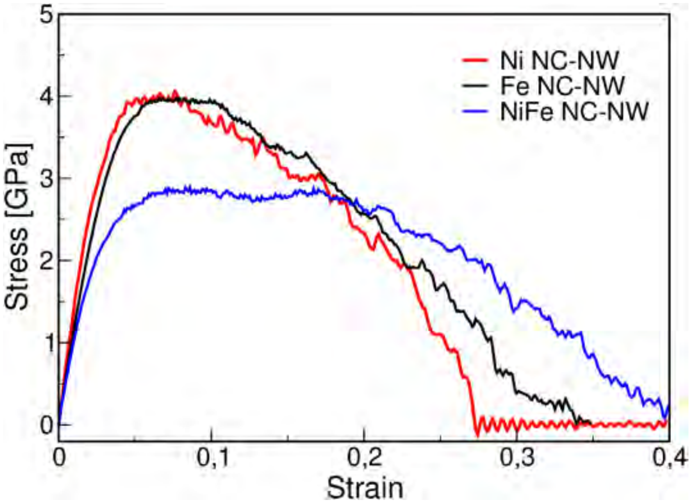

Figure 3.14: Stress- tensile strain curves for Ni, Fe, and NiFe polycrystalline NW.

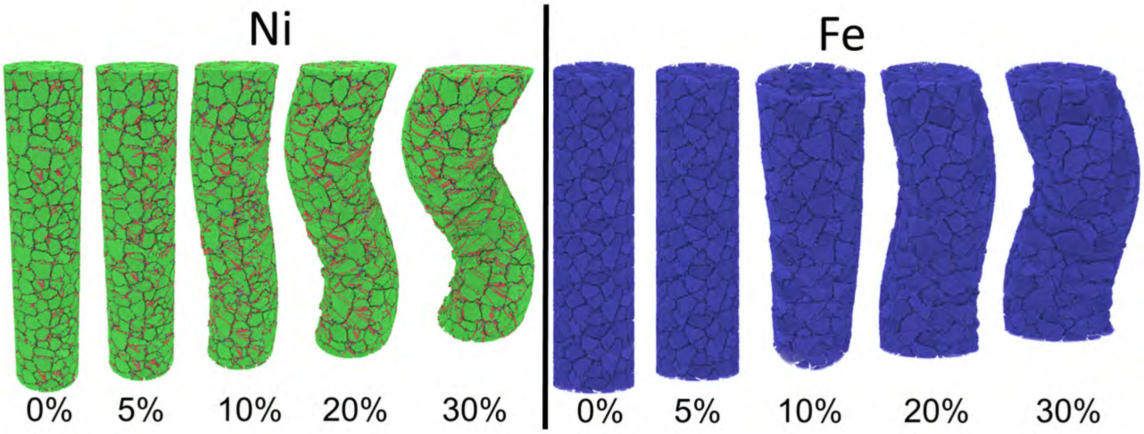

Figure 3.15: Snapshots of polycrystalline Ni and Fe NW under different applied compression strain. One of the major differences respect to the tensile strain process, is the coiling effect show in all cases, and getting clear after a 0.1 of strain.

the same structures and presented those results in Figures 3.15 and 3.16, for mono and bimetallic cases. This process followed the same procedure used in the previous section.

The stress-strain response is then presented in Figure 3.17, where the plastic zone shows a lower stress response of the bimetallic system. Besides this, if we consider the small strain regime, the Young moduli is higher follows the sequence Y(FeNi) < Y(Fe) < Y(Ni) under compression and tension, respectively. Additionally, it is clear from Figure 3.16 that all the defects are inside the Ni section, and no dislocation or stacking faults are present in Fe. Also, because of the coiling effect, we can see that there is a generation of stacking faults in the sections with higher curvature as it is possible to see in Figures 3.16 and 3.18. The only exception is again the Fe NW where the wider nanowires is due to the grain sliding.

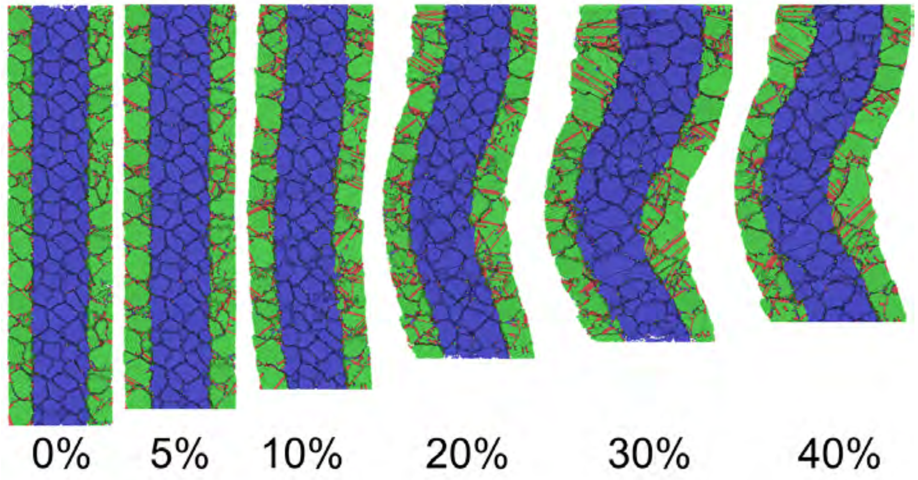

Figure 3.16: Snapshots of polycrystalline NiFe NW under different applied compression strain.

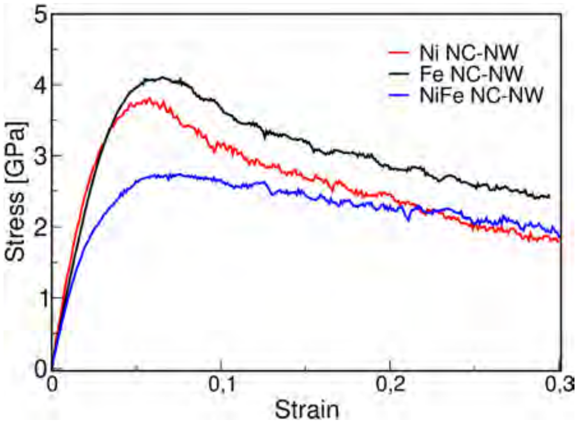

Figure 3.17: Stress- compression strain curves for Ni, Fe and NiFe polycrystalline NW.

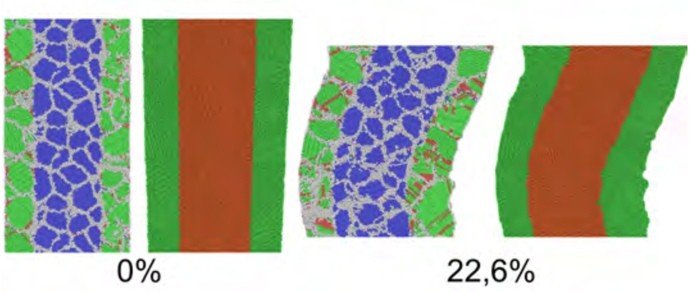

Figure 3.18: Snapshots of polycrystalline NiFe NW under different applied compression strain.

3.2.3 Discussions

From the simulations performed on mono and bimetallic nanowires we can identify an asymmetry in the mechanical response, when a tensile or compressive deformation are applied. This difference is also clear because for compression consider a coiling transformation that is not present during the tensile strain. Also, it is important to mention the increased plastic zone observed for the bimetallic FeNi system during the tensile strain, compared to the pure Ni and Fe NWs. This results emphasize the importance of the design of new materials, in order to modulate the mechanical response of these nanostructures.

General conclusions

Different bimetallic nanostructures were studied at different sizes, concentration, and elemental composition. The structures studied consider bimetallic nanoparticle systems and one-dimensional nanostructures.

The bimetallic nanoparticle systems were studied using annealing cycles over a collection of initial structures that allow the search of stable structures in the PES. The collection of structures were selected using a simplified energy model. The results using this methodology showed a relationship between the morphology, size, and concentration. In FeCu nanoparticles, the morphology of the lowest energy structures changed from core-shell to Janus as the size of the system and the Cu concentration increased. In AgCu systems, only core-shell structures were found as the most stable, but Janus morphologies reached similar energies for bigger nanoparticles. This theoretical results suggested the possibility to find coexistence between core-shell and Janus structures at large sizes, which was confirmed by experimental results. An additional bimetallic system, made of Fe and Ni, was studied to use the proposed methodology over atomic arrangements that prefer alloyed motifs in their bulk state. The result for this last system showed that the lowest energy structure also contains an alloy motif, but with a core-shell arrangement of $FeNi_3$@Fe.

Also, a novel energy potential, based on neural networks, was tested for Au nanoparticles against empirical potentials. The results with this new potential have more similarity to DFT energies, which allowed to find structures that empirical potentials missed.

Finally, mechanical properties of a bimetallic one-dimensional nanostructure were studied and compared against its monometallic counterparts. The mechanical properties of FeNi nanowires presented very different stress-strain curves, which does not behave like any of its monometallic components. The different behavior means that the bimetallic nanowire exhibited new mechanical properties compared with their mono-metallic counterparts due to a collective effect of both components.

In conclusion, bimetallic nanometric systems offer a possibility to tune the properties of the materials by changing their size and concentration.

All thesis goals were accomplished in the process:

- Different theoretical approaches were considered to explore the configuration landscape such as genetic algorithms, minimal hopping methods, and annealing, combined with embedded atom model potentials or first principle calculations.

- A simple energy model was used to support the selection of initial structures for our proposed exploration technique. These structures take the form of core-shell and Janus by using isolated or alloy configurations as building blocks. With this approach, successful matching with experimental data was achieved, in the particular cases of FeCu and AgCu.

- A phase diagram was obtained for the morphology of FeCu as a function of their size and concentration. Also, a reduction in energy differences between core-shell and Janus morphologies in AgCu system was found as their size increase.

- Mechanical and structural properties of bimetallic systems were studied using molecular dynamics (MD) simulations, obtaining efficiency improvement, respect to the monoatomic systems. Ni and Fe nanotubes and nanowires were considered getting an asymmetry in the mechanical response under tensile and compressive uniaxial strain.

- Additionally, a search using genetic algorithms combined with Neural Network trained potential has enabled us to find competing or more stable states than using classical potentials. This method was successfully applied to find stable Au clusters in the 30-80 atoms range.

With all these specific goals accomplished, it was possible the study of bimetallic systems resulting in two published articles [66, 83], and two more works to be published regarding the CuAg and FeNi nanoparticles. Also, regarding the nanostructure mechanical properties, another work was recently published with the study of Ni nanowires and nanotubes[177].

From this thesis, we expect to give a link between the study of small atomic clusters and the experimental evidence, using scalable methods to study nanometric size particles. This work could lead to the study of other characteristics from these atomic arrangements, such as energy barriers between different metastable morphologies.

Bibliography

[1] Rajib Ghosh Chaudhuri and Santanu Paria. Core/shell nanoparticles: Classes, properties, synthesis mechanisms, characterization, and applications. *Chemical Reviews*, 112(4):2373–2433, 2012. PMID: 22204603.

[2] Ph. Buffat and J-P. Borel. Size effect on the melting temperature of gold particles. *Phys. Rev. A*, 13:2287–2298, Jun 1976.

[3] R Kubo, A Kawabata, and S Kobayashi. Electronic properties of small particles. *Annual Review of Materials Science*, 14(1):49–66, 1984.

[4] W. P. Halperin. Quantum size effects in metal particles. *Reviews of Modern Physics*, 58(3):533–606, July 1986.

[5] Y. Volokitin, J. Sinzig, L. J. de Jongh, G. Schmid, M. N. Vargaftik, and I. I. Moiseevi. Quantum-size effects in the thermodynamic properties of metallic nanoparticles. *Nature*, 384(6610):621–623, dec 1996.

[6] A.R. Shafiqa, Azlan Abdul Aziz, and Baharak Mehrdel. Nanoparticle optical properties: Size dependence of a single gold spherical nanoparticle. *Journal of Physics: Conference Series*, 1083:012040, August 2018.

[7] Andrea R. Tao, Susan Habas, and Peidong Yang. Shape control of colloidal metal nanocrystals. *Small*, 4(3):310–325, March 2008.

[8] Pablo Díaz-Núñez, Guillermo González-Rubio, Alejandro Prada, Jesús González Izquierdo, Antonio Rivera, Luis Bañares, Andrés Guerrero-Martínez, and Ovidio Peña-Rodríguez. Using femtosecond laser irradiation to grow the belly of gold nanorods. *The Journal of Physical Chemistry C*, 122(34):19816–19822, August 2018.

[9] Dickson Joseph, Yun Suk Huh, and Young-Kyu Han. A top-down chemical approach to tuning the morphology and plasmon resonance of spiky nanostars for enriched SERS-based chemical sensing. *Sensors and Actuators B: Chemical*, 288:120–126, June 2019.

[10] K. Lance Kelly, Eduardo Coronado, Lin Lin Zhao, and George C. Schatz. The optical properties of metal nanoparticles: the influence of size, shape, and dielectric environment. *The Journal of Physical Chemistry B*, 107(3):668–677, January 2003.

[11] Xue Wang, Legna Figueroa-Cosme, Xuan Yang, Ming Luo, Jingyue Liu, Zhaoxiong Xie, and Younan Xia. Pt-based icosahedral nanocages: Using a combination of $\{111\}$ facets, twin defects, and ultrathin walls to greatly enhance their activity toward oxygen reduction. *Nano Letters*, 16(2):1467–1471, January 2016.

[12] Riccardo Ferrando, Julius Jellinek, and Roy L. Johnston. Nanoalloys: from theory to applications of alloy clusters and nanoparticles. *Chemical Reviews*, 108(3):845–910, mar 2008.

[13] Giovanni Barcaro, Alessandro Fortunelli, Giulia Rossi, Florin Nita, and Riccardo Ferrando. Electronic and structural shell closure in AgCu and AuCu nanoclusters. *The Journal of Physical Chemistry B*, 110(46):23197–23203, 2006. PMID: 17107165.

[14] Michel Pellarin, Inas Issa, Cyril Langlois, Marie-Ange Lebeault, Julien Ramade, Jean Lermé, Michel Broyer, and Emmanuel Cottancin. Plasmon spectroscopy and chemical structure of small bimetallic cu(1–x)agx clusters. *The Journal of Physical Chemistry C*, 119(9):5002–5012, feb 2015.

[15] Jia-Wen Hu, Jian-Feng Li, Bin Ren, De-Yin Wu, Shi-Gang Sun, and Zhong-Qun Tian. Palladium-coated gold nanoparticles with a controlled shell thickness used as surface-enhanced raman scattering substrate. *The Journal of Physical Chemistry C*, 111(3):1105–1112, 2007.

[16] Jiabao Ding, Lingzheng Bu, Shaojun Guo, Zipeng Zhao, Enbo Zhu, Yu Huang, and Xiaoqing Huang. Morphology and phase controlled construction of pt–ni nanostructures for efficient electrocatalysis. *Nano Letters*, 16(4):2762–2767, mar 2016.

[17] Remziye Güzel, Zafer Üstündağ, Haslet Ekşi, Selda Keskin, Bilge Taner, Zeynep Gülşah Durgun, Aybüke A. İsbir Turan, and Ali Osman Solak. Effect of au and au@ag core–shell nanoparticles on the SERS of bridging organic molecules. *Journal of Colloid and Interface Science*, 351(1):35 – 42, 2010.

[18] Liying Lu, Wentao Zhang, Dong Wang, Xiaoguang Xu, Jun Miao, and Yong Jiang. Fe@ag core–shell nanoparticles with both sensitive plasmonic properties and tunable magnetism. *Materials Letters*, 64(15):1732 – 1734, 2010.

[19] Luis M. Liz-Marzán. Tailoring surface plasmons through the morphology and assembly of metal nanoparticles. *Langmuir*, 22(1):32–41, 2006. PMID: 16378396.

[20] Jacqueline Quinn, Daniel Elliott, Suzanne O'Hara, and Alexa Billow. Use of nanoscale iron and bimetallic particles for environmental remediation: A review of field-scale applications. In *ACS Symposium Series*, pages 263–283. American Chemical Society, dec 2009.

[21] Sibin Duan and Rongming Wang. Bimetallic nanostructures with magnetic and noble metals and their physicochemical applications. *Progress in Natural Science: Materials International*, 23(2):113–126, apr 2013.

[22] Xiangwen Liu, Dingsheng Wang, and Yadong Li. Synthesis and catalytic properties of bimetallic nanomaterials with various architectures. *Nano Today*, 7(5):448 – 466, 2012.

[23] Gaurav Sharma, Amit Kumar, Shweta Sharma, Mu. Naushad, Ram Prakash Dwivedi, Zeid A. ALOthman, and Genene Tessema Mola. Novel development of nanoparticles to bimetallic nanoparticles and their composites: A review. *Journal of King Saud University - Science*, 31(2):257–269, April 2019.

[24] Hao Lv, Yang Wang, Aaron Lopes, Dongdong Xu, and Ben Liu. Ultrathin PdAg single-crystalline nanowires enhance ethanol oxidation electrocatalysis. *Applied Catalysis B: Environmental*, 249:116–125, July 2019.

[25] Hao Lv, Xin Chen, Dongdong Xu, Yichen Hu, Haoquan Zheng, Steven L. Suib, and Ben Liu. Ultrathin pdpt bimetallic nanowires with enhanced electrocatalytic performance for hydrogen evolution reaction. *Applied Catalysis B: Environmental*, 238:525 – 532, 2018.

[26] Ronggen Cao and Chuang Deng. The ultra-small strongest grain size in nanocrystalline ni nanowires. *Scripta Materialia*, 94:9–12, January 2015.

[27] A.G.N. Sofiah, M. Samykano, K. Kadirgama, R.V. Mohan, and N.A.C. Lah. Metallic nanowires: Mechanical properties – theory and experiment. *Applied Materials Today*, 11:320–337, June 2018.

[28] Xun Hong, Dingsheng Wang, Rong Yu, Hui Yan, Yi Sun, Lin He, Zhiqian Niu, Qing Peng, and Yadong Li. Ultrathin Au–Ag bimetallic nanowires with coulomb blockade effects. *Chem. Commun.*, 47:5160–5162, 2011.

[29] Nitin K. Chaudhari, Jinwhan Joo, Byeongyoon Kim, Bibi Ruqia, Sang-Il Choi, and Kwangyeol Lee. Recent advances in electrocatalysts toward the oxygen reduction reaction: the case of PtNi octahedra. *Nanoscale*, 10(43):20073–20088, 2018.

[30] Frank H. Stillinger. Exponential multiplicity of inherent structures. *Physical Review E*, 59(1):48–51, jan 1999.

[31] Y. Lu, C. Peng, Y. Ganesan, J. Y. Huang, and J. Lou. Quantitative in situ tem tensile testing of an individual nickel nanowire. *Nanotechnology*, 22(35):355702, 2011.

[32] N AgraÃ¯t. Quantum properties of atomic-sized conductors. *Physics Reports*, 377(2-3):81–279, April 2003.

[33] M. S. Dresselhaus, G. Chen, M. Y. Tang, R. G. Yang, H. Lee, D. Z. Wang, Z. F. Ren, J.-P. Fleurial, and P. Gogna. New directions for low-dimensional thermoelectric materials. *Advanced Materials*, 19(8):1043–1053, March 2007.

[34] C. M. Lieber. Nanoscale science and technology: Building a big future from small things. *Materials Research Society Bulletin*, 28:486–491, 2003.

[35] Ludovico Cademartiri and Geoffrey A. Ozin. Ultrathin nanowires-a materials chemistry perspective. *Advanced Materials*, 21(9):1013–1020, March 2009.

[36] Francesca Baletto. Structural properties of sub-nanometer metallic clusters. *Journal of Physics: Condensed Matter*, 31(11):113001, jan 2019.

[37] Jörg Behler and Michele Parrinello. Generalized neural-network representation of high-dimensional potential-energy surfaces. *Physical Review Letters*, 98(14), apr 2007.

[38] Si-Da Huang, Cheng Shang, Xiao-Jie Zhang, and Zhi-Pan Liu. Material discovery by combining stochastic surface walking global optimization with a neural network. *Chemical Science*, 8(9):6327–6337, 2017.

[39] C. C. J. Roothaan. New developments in molecular orbital theory. *Rev. Mod. Phys.*, 23:69–89, Apr 1951.

[40] P. Hohenberg and W. Kohn. Inhomogeneous electron gas. *Physical Review*, 136(3B):B864–B871, nov 1964.

[41] John P. Perdew, Kieron Burke, and Matthias Ernzerhof. Generalized gradient approximation made simple. *Physical Review Letters*, 77(18):3865–3868, oct 1996.

[42] John P. Perdew, Kieron Burke, and Matthias Ernzerhof. Generalized gradient approximation made simple [phys. rev. lett. 77, 3865 (1996)]. *Phys. Rev. Lett.*, 78:1396–1396, Feb 1997.

[43] Matthias Ernzerhof and Gustavo E. Scuseria. Assessment of the perdew–burke–ernzerhof exchange-correlation functional. *The Journal of Chemical Physics*, 110(11):5029–5036, mar 1999.

[44] Neil W. Ashcroft and N. David Mermin. *Solid State Physics*. Cengage Learning, 1976.

[45] Murray S. Daw, Stephen M. Foiles, and Michael I. Baskes. The embedded-atom method: a review of theory and applications. *Materials Science Reports*, 9(7-8):251–310, mar 1993.

[46] T.M. Mitchell. *Machine Learning*. McGraw-Hill International Editions. McGraw-Hill, 1997.

[47] Ian J. Goodfellow, Nate Koenig, Marius Muja, Caroline Pantofaru, Alexander Sorokin, and Leila Takayama. Help me help you: Interfaces for personal robots. In *Proceedings of the 5th ACM/IEEE International Conference on Human-robot Interaction*, HRI '10, pages 187–188, Piscataway, NJ, USA, 2010. IEEE Press.

[48] Geoffrey Hinton, Li Deng, Dong Yu, George Dahl, Abdel rahman Mohamed, Navdeep Jaitly, Andrew Senior, Vincent Vanhoucke, Patrick Nguyen, Tara Sainath, and Brian Kingsbury. Deep neural networks for acoustic modeling in speech recognition: The shared views of four research groups. *IEEE Signal Processing Magazine*, 29(6):82–97, nov 2012.

[49] Ilya Sutskever, Oriol Vinyals, and Quoc V. Le. Sequence to sequence learning with neural networks, 2014.

[50] Dzmitry Bahdanau, Kyunghyun Cho, and Yoshua Bengio. Neural machine translation by jointly learning to align and translate, 2014.

[51] Samad Hajinazar, Junping Shao, and Aleksey N. Kolmogorov. Stratified construction of neural network based interatomic models for multicomponent materials. *Physical Review B*, 95(1), jan 2017.

[52] Bernd Hartke. Global optimization. *Wiley Interdisciplinary Reviews: Computational Molecular Science*, 1(6):879–887, May 2011.

[53] David J. Wales and Jonathan P. K. Doye. Global optimization by basin-hopping and the lowest energy structures of lennard-jones clusters containing up to 110 atoms. *The Journal of Physical Chemistry A*, 101(28):5111–5116, jul 1997.

[54] Masao Iwamatsu and Yutaka Okabe. Basin hopping with occasional jumping. *Chemical Physics Letters*, 399(4-6):396–400, dec 2004.

[55] Roy L. Johnston. Evolving better nanoparticles: Genetic algorithms for optimising cluster geometries. *Dalton Transactions*, 22:4193, 2003.

[56] Stefan Goedecker. Minima hopping: An efficient search method for the global minimum of the potential energy surface of complex molecular systems. *The Journal of Chemical Physics*, 120(21):9911–9917, jun 2004.

[57] Shantanu Roy, Stefan Goedecker, and Vladimir Hellmann. Bell-evans-polanyi principle for molecular dynamics trajectories and its implications for global optimization. *Physical Review E*, 77(5), may 2008.

[58] Sandro E. Schönborn, Stefan Goedecker, Shantanu Roy, and Artem R. Oganov. The performance of minima hopping and evolutionary algorithms for cluster structure prediction. *The Journal of Chemical Physics*, 130(14):144108, apr 2009.

[59] S. Kirkpatrick, C. D. Gelatt, and M. P. Vecchi. Optimization by simulated annealing. *Science*, 220(4598):671–680, may 1983.

[60] S. Pal, Y. K. Tak, and J. M. Song. Does the antibacterial activity of silver nanoparticles depend on the shape of the nanoparticle? a study of the gram-negative bacterium escherichia coli. *Applied and Environmental Microbiology*, 73(6):1712–1720, jan 2007.

[61] Kaitlin M. Bratlie, Hyunjoo Lee, Kyriakos Komvopoulos, Peidong Yang, and Gabor A. Somorjai. Platinum nanoparticle shape effects on benzene hydrogenation selectivity. *Nano Letters*, 7(10):3097–3101, oct 2007.

[62] Beatriz Roldan Cuenya. Synthesis and catalytic properties of metal nanoparticles: Size, shape, support, composition, and oxidation state effects. *Thin Solid Films*, 518(12):3127–3150, apr 2010.

[63] Steve Plimpton. Fast parallel algorithms for short-range molecular dynamics. *Journal of Computational Physics*, 117(1):1–19, mar 1995.

[64] N.P. Gupta. On the lindemann law of melting of solids. *Solid State Communications*, 13(1):69–71, July 1973.

[65] M. A. Turchanin, P. G. Agraval, and I. V. Nikolaenko. Thermodynamics of alloys and phase equilibria in the copper-iron system. *Journal of Phase Equilibria*, 24(4):307–319, jul 2003.

[66] Javier Rojas-Nunez, Rafael I. Gonzalez, Eduardo M. Bringa, Sebastian Allende, Pamela Sepúlveda, Nicolás Arancibia-Miranda, and Samuel E. Baltazar. Toward controlled morphology of FeCu nanoparticles: Cu concentration and size effects. *The Journal of Physical Chemistry C*, 122(15):8528–8534, 2018.

[67] G. Bonny, R.C. Pasianot, N. Castin, and L. Malerba. Ternary fe–cu–ni many-body potential to model reactor pressure vessel steels: First validation by simulated thermal annealing. *Philosophical Magazine*, 89(34-36):3531–3546, dec 2009.

[68] Y. Mishin, M. J. Mehl, D. A. Papaconstantopoulos, A. F. Voter, and J. D. Kress. Structural stability and lattice defects in copper:ab initio, tight-binding, and embedded-atom calculations. *Physical Review B*, 63(22), may 2001.

[69] Alexander Stukowski. Visualization and analysis of atomistic simulation data with OVITO–the open visualization tool. *Modelling and Simulation in Materials Science and Engineering*, 18(1):015012, dec 2009.

[70] S. Bel Haj Salah, C. Gerard, and L. Pizzagalli. Influence of surface atomic structure on the mechanical response of aluminum nanospheres under compression. *Computational Materials Science*, 129:273–278, mar 2017.

[71] Christopher R. Weinberger and Wei Cai. Plasticity of metal nanowires. *Journal of Materials Chemistry*, 22(8):3277, 2012.

[72] A. Stukowski, K. Albe, and D. Farkas. Nanotwinned fcc metals: Strengthening versus softening mechanisms. *Physical Review B*, 82(22), dec 2010.

[73] A. Suzuki and Y. Mishin. Atomistic modeling of point defects and diffusion in copper grain boundaries. *Interface Science*, 11(1):131–148, 2003.

[74] John Price Hirth and Jens Lothe. *Theory of Dislocations*. Krieger Publishing Company, 1992.

[75] M. I. Mendelev, S. Han, D. J. Srolovitz, G. J. Ackland, D. Y. Sun, and M. Asta. Development of new interatomic potentials appropriate for crystalline and liquid iron. *Philosophical Magazine*, 83(35):3977–3994, dec 2003.

[76] G. Sainath and B.K. Choudhary. Molecular dynamics simulations on size dependent tensile deformation behaviour of [110] oriented body centred cubic iron nanowires. *Materials Science and Engineering: A*, 640:98–105, jul 2015.

[77] Yang Lu, Jun Song, Jian Yu Huang, and Jun Lou. Surface dislocation nucleation mediated deformation and ultrahigh strength in sub-10-nm gold nanowires. *Nano Research*, 4(12):1261–1267, oct 2011.

[78] Yanlai Han and Weile Yan. Bimetallic nickel–iron nanoparticles for groundwater decontamination: Effect of groundwater constituents on surface deactivation. *Water Research*, 66:149–159, dec 2014.

[79] K. Lu, L. Lu, and S. Suresh. Strengthening materials by engineering coherent internal boundaries at the nanoscale. *Science*, 324(5925):349–352, apr 2009.

[80] Z. Budrovic. Plastic deformation with reversible peak broadening in nanocrystalline nickel. *Science*, 304(5668):273–276, apr 2004.

[81] Subin Lee, Jiseong Im, Youngdong Yoo, Erik Bitzek, Daniel Kiener, Gunther Richter, Bongsoo Kim, and Sang Ho Oh. Reversible cyclic deformation mechanism of gold nanowires by twinning–detwinning transition evidenced from in situ TEM. *Nature Communications*, 5(1), jan 2014.

[82] K. Kang, J. Wang, and I. J. Beyerlein. Atomic structure variations of mechanically stable fcc-bcc interfaces. *Journal of Applied Physics*, 111(5):053531, mar 2012.

[83] Pamela Sepúlveda, María A. Rubio, Samuel E. Baltazar, J. Rojas-Nunez, J.L. Sánchez Llamazares, Alejandra García Garcia, and Nicolás Arancibia-Miranda. As(v) removal capacity of FeCu bimetallic nanoparticles in aqueous solutions: The influence of cu content and morphologic changes in bimetallic nanoparticles. *Journal of Colloid and Interface Science*, 524:177–187, aug 2018.

[84] Chuan-Bao Wang and Wei xian Zhang. Synthesizing nanoscale iron particles for rapid and complete dechlorination of TCE and PCBs. *Environmental Science & Technology*, 31(7):2154–2156, jul 1997.

[85] Kang Xiao, Zhenghong Bao, Xingzhen Qi, Xinxing Wang, Liangshu Zhong, Minggui Lin, Kegong Fang, and Yuhan Sun. Unsupported CuFe bimetallic nanoparticles for higher alcohol synthesis via syngas. *Catalysis Communications*, 40:154–157, oct 2013.

[86] Kang Xiao, Zhenghong Bao, Xingzhen Qi, Xinxing Wang, Liangshu Zhong, Kegong Fang, Minggui Lin, and Yuhan Sun. Structural evolution of CuFe bimetallic nanoparticles for higher alcohol synthesis. *Journal of Molecular Catalysis A: Chemical*, 378:319–325, nov 2013.

[87] Paulin Buchwalter, Jacky Rosé, and Pierre Braunstein. Multimetallic catalysis based on heterometallic complexes and clusters. *Chemical Reviews*, 115(1):28–126, December 2014.

[88] Frederick H. Hayes, Hans Leo Lukas, Guenter Effenberg, and Guenter Petzow. Thermodynamic optimisation of the Cu-Ag-Pb system. *Zeitschrift fuer Metallkunde/Materials Research and Advanced Techniques*, 77:749–754, 11 1986.

[89] S. Núñez and R. L. Johnston. Structures and chemical ordering of small cu-ag clusters. *The Journal of Physical Chemistry C*, 114(31):13255–13266, July 2010.

[90] Go Kawamura, Samuel Alvarez, Ian E. Stewart, Matthew Catenacci, Zuofeng Chen, and Yoon-Cheol Ha. Production of oxidation-resistant cu-based nanoparticles by wire explosion. *Scientific Reports*, 5(1), December 2015.

[91] Changsoo Lee, Na Rae Kim, Jahyun Koo, Yung Jong Lee, and Hyuck Mo Lee. Cu-ag core–shell nanoparticles with enhanced oxidation stability for printed electronics. *Nanotechnology*, 26(45):455601, oct 2015.

[92] Kihyun Shin, Da Hye Kim, Sang Chul Yeo, and Hyuck Mo Lee. Structural stability of agcu bimetallic nanoparticles and their application as a catalyst: A dft study. *Catalysis Today*, 185(1):94 – 98, 2012. Catalysis on Energy and Environmental Technologies: 13th Korea-Japan Symposium on Catalysis.

[93] P L Williams, Y Mishin, and J C Hamilton. An embedded-atom potential for the cu–ag system. *Modelling and Simulation in Materials Science and Engineering*, 14(5):817–833, may 2006.

[94] Yongsheng Yu, Weiwei Yang, Xiaolian Sun, Wenlei Zhu, X.-Z. Li, D. J. Sellmyer, and Shouheng Sun. Monodisperse MPt (m = fe, co, ni, cu, zn) nanoparticles prepared from a facile oleylamine reduction of metal salts. *Nano Letters*, 14(5):2778–2782, April 2014.

[95] Eunjin Choi, Sohee Lee, and Yuanzhe Piao. A solventless mix–bake–wash approach to the facile controlled synthesis of core–shell and alloy ag–cu bimetallic nanoparticles. *CrystEngComm*, 17(31):5940–5946, 2015.

[96] Nafiseh Moghimi, Fatemeh Rahnemaye Rahsepar, Saurabh Srivastava, Nina Heinig, and Kam Tong Leung. Shape-dependent magnetism of bimetallic FeNi nanosystems. *Journal of Materials Chemistry C*, 2(31):6370, July 2014.

[97] Yan Liu, Yanxiu Chi, Shiyao Shan, Jun Yin, Jin Luo, and Chuan-Jian Zhong. Characterization of magnetic nife nanoparticles with controlled bimetallic composition. *Journal of Alloys and Compounds*, 587:260 – 266, 2014.

[98] Juhani Teeriniemi, Marko Melander, Saana Lipasti, Richard Hatz, and Kari Laasonen. Fe–ni nanoparticles: A multiscale first-principles study to predict geometry, structure, and catalytic activity. *The Journal of Physical Chemistry C*, 121(3):1667–1674, January 2017.

[99] V. Torabinejad, M. Aliofkhazraei, S. Assareh, M.H. Allahyarzadeh, and A. Sabour Rouhaghdam. Electrodeposition of ni-fe alloys, composites, and nano coatings–a review. *Journal of Alloys and Compounds*, 691:841 – 859, 2017.

[100] Peter Schwerdtfeger, Michael Dolg, W. H. Eugen Schwarz, Graham A. Bowmaker, and Peter D. W. Boyd. Relativistic effects in gold chemistry. i. diatomic gold compounds. *The Journal of Chemical Physics*, 91(3):1762–1774, 1989.

[101] M. Haruta. Size- and support-dependency in the catalysis of gold. *Catalysis Today*, 36:153–166, 1997.

[102] H. Hakkinen. Atomic and electronic structure of gold clusters: understanding flakes, cages and superatoms from simple concepts. *Chem Soc Rev*, 37(9):1847–59, 2008.

[103] N. Jabr and A. Kodlaa. Dft study of small gold clusters aun (n=2-13): The structural, electronic, thermodynamic and spectral properties. *Chemistry and Materials Research*, 9:17–28, 2017.

[104] J. M. Soler, I. L. Garzón, and J. D. Joannopoulos. Structural patterns of unsupported gold clusters. *Solid State Communications*, 117:621–625, 2001.

[105] Mikael P. Johansson, Dage Sundholm, and Juha Vaara. Au32: A 24-carat golden fullerene. *Angewandte Chemie International Edition*, 43(20):2678–2681, 2004.

[106] R. Ouyang, Y. Xie, and D. E. Jiang. Global minimization of gold clusters by combining neural network potentials and the basin-hopping method. *Nanoscale*, 7(36):14817–14821, 2015.

[107] N. Tarrat, M. Rapacioli, and F. Spiegelman. Au147 nanoparticles: Ordered or amorphous? *J. Chem. Phys.*, 148(20):204308, 2018.

[108] Ajanta Deka and Ramesh C. Deka. Structural and electronic properties of stable aun (n=2–13) clusters: A density functional study. *Journal of Molecular Structure: THEOCHEM*, 870(1-3):83–93, 2008.

[109] P. Pyykko. Theoretical chemistry of gold. III. *Chem Soc Rev*, 37(9):1967–97, 2008.

[110] K. Michaelian, N. Rendón, and I. L. Garzón. Structure and energetics of Ni, Ag, and Au nanoclusters. *Physical Review B*, 60:2000–2010, 1999.

[111] Samad Hajinazar, Ernesto D. Sandoval, Aiden J. Cullo, and Aleksey N. Kolmogorov. Multitribe evolutionary search for stable cu–pd–ag nanoparticles using neural network models. *Phys. Chem. Chem. Phys.*, 21:8729–8742, 2019.

[112] Xia Wu and Yan Sun. Stable structures and potential energy surface of the metallic clusters: Ni, cu, ag, au, pd, and pt. *Journal of Nanoparticle Research*, 19(6):201, Jun 2017.

[113] Pär A. T. Olsson. Transverse resonant properties of strained gold nanowires. *Journal of Applied Physics*, 108(3):034318, 2010.

[114] Georg Kresse and Jürgen Furthmüller. Efficient iterative schemes for ab initio total-energy calculations using a plane-wave basis set. *Physical review B*, 54(16):11169, 1996.

[115] G. Kresse and J. Hafner. Ab initiomolecular dynamics for liquid metals. *Physical Review B*, 47(1):558–561, 1993.

[116] P. E. Blöchl. Projector augmented-wave method. *Phys. Rev. B*, 50:17953–17979, Dec 1994.

[117] Hendrik J. Monkhorst and James D. Pack. Special points for brillouin-zone integrations. *Phys. Rev. B*, 13:5188–5192, Jun 1976.

[118] T. Pilati and A. Forni. Symmol: a program to find the maximum symmetry group in an atom cluster, given a prefixed tolerance. *J. Appl. Cryst.*, 31:503–504, 1998.

[119] D. Schebarchov, F. Baletto, and D. J. Wales. Structure, thermodynamics, and rearrangement mechanisms in gold clusters-insights from the energy landscapes framework. *Nanoscale*, 10(4):2004–2016, 2018.

[120] S. Chiriki, S. Jindal, and S. S. Bulusu. Neural network potentials for dynamics and thermodynamics of gold nanoparticles. *J Chem Phys*, 146(8):084314, 2017.

[121] Maurício J. Piotrowski, Crina G. Ungureanu, Polina Tereshchuk, Krys E. A. Batista, Anderson S. Chaves, Diego Guedes-Sobrinho, and Juarez L. F. Da Silva. Theoretical study of the structural, energetic, and electronic properties of 55-atom metal nanoclusters: A dft investigation within van der waals corrections, spin–orbit coupling, and PBE+U of 42 metal systems. *The Journal of Physical Chemistry C*, 120(50):28844–28856, 2016.

[122] P. Garcia-Mochales, R. Paredes, S. Pelaez, and P. A. Serena. Statistical analysis of the breaking processes of ni nanowires. *Nanotechnology*, 19(22):225704, 2008.

[123] J. Verbeeck, O. I. Lebedev, G. Van Tendeloo, L. Cagnon, C. Bougerol, and G. Tourillon. Fe and co nanowires and nanotubes synthesized by template electrodeposition. *Journal of the Electrochemical Society*, 150:E468–E471, 2003.

[124] P. S. Branicio and J.P. Rino. Large deformation and amorphization of ni nanowires under uniaxial strain: A molecular dynamics study. *Physical Review B*, 62:16950–16955, 2000.

[125] Ajing Cao, Yueguang Wei, and Scott X. Mao. Alternating starvation of dislocations during plastic yielding in metallic nanowires. *Scripta Materialia*, 59(2):219–222, 2008.

[126] R. Cao, Y. Deng, and C. Deng. Ultrahigh plastic flow in au nanotubes enabled by surface stress facilitated reconstruction. *Acta Materialia*, 86:15–22, 2015.

[127] H. Ikeda, T. Cagin, K. Samwer, W. L. Johnson, and W. A. Goddard III. Strain rate induced amorphization in metallic nanowires. *Physical Review Letters*, 82:2900–2903, 1999.

[128] Changjiang Ji and Harold S. Park. Characterizing the elasticity of hollow metal nanowires. *Nanotechnology*, 18(11):115707, 2007.

[129] Dan Huang, Qing Zhang, and Pizhong Qiao. Molecular dynamics evaluation of strain rate and size effects on mechanical properties of fcc nickel nanowires. *Computational Materials Science*, 50(3):903–910, 2011.

[130] Brandon B. Seo, Junhua Gu, Zeinab Jahed, and Ting Y. Tsui. Influence of grain boundary modifier on the strength size-dependence displayed by complex-shaped nanocrystalline nickel pillars. *Thin Solid Films*, 621:178–183, 2017.

[131] Shuozhi Xu and Saeed Zare Chavoshi. Uniaxial deformation of nanotwinned nanotubes in body-centered cubic tungsten. *Current Applied Physics*, 18(1):114–121, 2018.

[132] Lihua Wang, Yan Lu, Deli Kong, Lirong Xiao, Xuechao Sha, Jialin Sun, Ze Zhang, and Xiaodong Han. Dynamic and atomic-scale understanding of the twin thickness effect on dislocation nucleation and propagation activities by in situ bending of ni nanowires. *Acta Materialia*, 90:194–203, 2015.

[133] H. Choi and S. H. Park. Seedless growth of free-standing copper nanowires by chemical vapor deposition. *Journal of the American Chemical Society*, 126:6248–6249, 2004.

[134] A. Pereira, J. L. Palma, M. Vazquez, J. C. Denardin, and J. Escrig. A soft/hard magnetic nanostructure based on multisegmented coni nanowires. *Phys Chem Chem Phys*, 17(7):5033–8, 2015.

[135] J. Shui and J. C. M. Li. Platinum nanowires produced by electrospinning. *Nano Letters*, 9:1307–1314, 2009.

[136] Y. Chen, C. Xu, Y. Zhou, K. Maaz, H. Yao, D. Mo, S. Lyu, J. Duan, and J. Liu. Temperature- and angle-dependent magnetic properties of ni nanotube arrays fabricated by electrodeposition in polycarbonate templates. *Nanomaterials*, 6(12):231, 2016.

[137] Z. X. Wu, Y. W. Zhang, M. H. Jhon, and D. J. Srolovitz. Anatomy of nanomaterial deformation: Grain boundary sliding, plasticity and cavitation in nanocrystalline ni. *Acta Materialia*, 61(15):5807–5820, 2013.

[138] J. B. Bilde-Sorensen and J. Schiotz. Nanocrystals get twins. *Science*, 300:1244–1245, 2003.

[139] E. M. Bringa, A. Caro, Y. Wang, M. Victoria, J. M. McNaney, B. A. Remington, R. F. Smith, B. R. Torralva, and H. Van Swygenhoven. Ultrahigh strength in nanocrystalline materials under shock loading. *Science*, 309(5742):1838–1841, 2005.

[140] A. Hasnaoui, H. Van Swygenhoven, and P. M. Derlet. Dimples on nanocrystalline fracture surfaces as evidence for shear plane formation. *Science*, 300:1550–1552, 2003.

[141] S. Plimpton. Fast parallel algorithms for short–range molecular dynamics. *Journal of Computational Physics*, 117:1–19, 1995.

[142] M. S. Daw and M. I. Baskes. Embedded-atom method: Derivation and application to impurities, surfaces, and other defects in metals. *Physical Review B*, 29:6443–6453, 1983.

[143] Y. Mishin, D. Farkas, M. J. Mehl, and D. A. Papaconstantopoulos. Interatomic potentials for monoatomic metals from experimental data and ab initio calculations. *Physical Review B*, 59:3393–3407, 1999.

[144] A. Alavi, K. Mirabbaszadeh, P. Nayebi, and E. Zaminpayma. Molecular dynamics simulation of mechanical properties of ni–al nanowires. *Computational Materials Science*, 50(1):10–14, 2010.

[145] R. Dingreville and J. Qu. A semi-analytical method to compute surface elastic properties. *Acta Materialia*, 55(1):141–147, 2007.

[146] H. N. Jarmakani, E. M. Bringa, P. Erhart, B. A. Remington, Y. M. Wang, N. Q. Vo, and M. A. Meyers. Molecular dynamics simulations of shock compression of nickel: From monocrystals to nanocrystals. *Acta Materialia*, 56(19):5584–5604, 2008.

[147] Z. X. Wu, Y. W. Zhang, M. H. Jhon, J. R. Greer, and D. J. Srolovitz. Nanostructure and surface effects on yield in cu nanowires. *Acta Materialia*, 61(6):1831–1842, 2013.

[148] J. A. Zimmerman, H. Gao, and F. F. Abraham. Generalized stacking fault energies for embedded atom fcc metals. *Modelling and Simulation in Materials Science and Engineering*, 8:103–115, 2000.

[149] Nina Gunkelmann, Eduardo M. Bringa, Keonwook Kang, Graeme J. Ackland, Carlos J. Ruestes, and Herbert M. Urbassek. Polycrystalline iron under compression: Plasticity and phase transitions. *Physical Review B*, 86(14):144111, 2012.

[150] Felipe J. Valencia, Rafael I. González, Eduardo M. Bringa, and Miguel Kiwi. Hillock formation on nanocrystalline diamond. *Carbon*, 119:219–224, 2017.

[151] Felipe Valencia, José D. Mella, Rafael I. González, Miguel Kiwi, and Eduardo M. Bringa. Confinement effects in irradiation of nanocrystalline diamond. *Carbon*, 93:458–464, 2015.

[152] A. Stukowski. Structure identification methods for atomistic simulations of crystalline materials. *Modelling and Simulation in Materials Science and Engineering*, 20:045021, 2012.

[153] A. Stukowski. Visualization and analysis of atomistic simulation data with ovito–the open visualization tool. *Modelling and Simulation in Materials Science and Engineering*, 18:015012, 2010.

[154] Z. R. Liu and R. F. Zhang. Aacsd: An atomistic analyzer for crystal structure and defects. *Computer Physics Communications*, 222:229–239, 2018.

[155] N. Q. Vo, R. S. Averback, P. Bellon, S. Odunuga, and A. Caro. Quantitative description of plastic deformation in nanocrystalline cu: Dislocation glide versus grain boundary sliding. *Physical Review B*, 77(13):134108, 2008.

[156] L. R. Meza, S. Das, and J. R. Greer. Strong, lightweight, and recoverable three-dimensional ceramic nanolattices. *Science*, 345:1322–1326, 2014.

[157] X. Zheng, W. Smith, J. Jackson, B. Moran, H. Cui, D. Chen, J. Ye, N. Fang, N. Rodriguez, T. Weisgraber, and C. M. Spadaccini. Multiscale metallic metamaterials. *Nat Mater*, 15(10):1100–6, 2016.

[158] Dinc Erdeniz, Tobias A. Schaedler, and David C. Dunand. Deposition-based synthesis of nickel-based superalloy microlattices. *Scripta Materialia*, 138:28–31, 2017.

[159] T. A. Schaedler, C. J. Ro, A. E. Sorensen, Z. Eckel, S. S. Yang, W. B. Carter, and A. J. Jacobsen. Designing metallic microlattices for energy absorber applications. *Advanced Engineering Materials*, 16(3):276–283, 2014.

[160] A. Torrents, T. A. Schaedler, A. J. Jacobsen, W. B. Carter, and L. Valdevit. Characterization of nickel-based microlattice materials with structural hierarchy from the nanometer to the millimeter scale. *Acta Materialia*, 60(8):3511–3523, 2012.

[161] Lorenzo Valdevit, Scott W. Godfrey, Tobias A. Schaedler, Alan J. Jacobsen, and William B. Carter. Compressive strength of hollow microlattices: Experimental characterization, modeling, and optimal design. *Journal of Materials Research*, 28(17):2461–2473, 2013.

[162] L. C. Montemayor and J. R. Greer. Mechanical response of hollow metallic nanolattices: Combining structural and material size effects. *Journal of Applied Mechanics*, 82(7), 2015.

[163] H. S. Park, K. Gall, and J. A. Zimmerman. Deformation of fcc nanowires by twinning and slip. *Journal of the Mechanics and Physics of Solids*, 54(9):1862–1881, 2006.

[164] A. R. Setoodeh, H. Attariani, and M. Khosrownejad. Nickel nanowires under uniaxial loads: A molecular dynamics simulation study. *Computational Materials Science*, 44(2):378–384, 2008.

[165] B. Wang, D. Shi, J. Jia, G. Wang, X. Chen, and J. Zhao. Elastic and plastic deformations of nickel nanowires under uniaxial compression. *Physica E: Low-dimensional Systems and Nanostructures*, 30(1-2):45–50, 2005.

[166] K. Zhou, B. Liu, S. Shao, and Y. Yao. Molecular dynamics simulations of tension–compression asymmetry in nanocrystalline copper. *Physics Letters A*, 381(13):1163–1168, 2017.

[167] L. P. Lefebvre, J. Banhart, and D. C Dunand. Porous metals and metallic foams: Current status and recent developments. *Advanced Engineering Materials*, 10(9):775–787, 2008.

[168] Ashwin Ramasubramaniam and Emily A. Carter. Coupled quantum–atomistic and quantum–continuum mechanics methods in materials research. *MRS Bulletin*, 32(11):913–918, 2011.

[169] J. Monk and D. Farkas. Tension–compression asymmetry and size effects in nanocrystalline ni nanowires. *Philosophical Magazine*, 87(14-15):2233–2244, 2007.

[170] G Simmons and H. Wang. *Single Crystal Elastic Constants and Calculated Aggregate Properties: A Handbook*. Cambridge, The MIT Press, second edition edition, 1971.

[171] L. E. Murr. *Interfacial Phenomena in Metals and Alloys*. Addison-Wesley, 1975.

[172] R. J. Birgeneau, J. Cordes, G. Dolling, and A. D. B. Woods. Normal modes of vibration in nickel. *Physical Review*, 136:A1359–A1365, 1964.

[173] E. M. Bringa, J. D. Monk, A. Caro, A. Misra, L. Zepeda-Ruiz, M. Duhaineau, F. Abraham, M. Nastasi, S. T. Picraux, Y. Q. Wang, and D. Farkas. Are nanoporous materials radiation resistant? *Nano Letters*, 12:3351–3355, 2011.

[174] J. H. Song, F. Kim, D. Kim, and P. Yang. Crystal overgrowth on gold nanorods: tuning the shape, facet, aspect ratio, and composition of the nanorods. *Chemistry*, 11(3):910–916, 2005.

[175] V. Borysiuk and I. Lyashenko. Modeling of the elastic properties of the core-shell au-ag nanorod. In *2016 IEEE 36th International Conference on Electronics and Nanotechnology (ELNANO)*, pages 118–120, 2016.

[176] G. Bonny, R. C. Pasianot, N. Castin, and L. Malerba. Ternary fe–cu–ni many-body potential to model reactor pressure vessel steels: First validation by simulated thermal annealing. *Philosophical Magazine*, 89(34-36):3531–3546, 2009.

[177] Javier Rojas-Nunez, Felipe Valencia, Rafael I. Gonzalez, Eduardo M. Bringa, Sebastian Allende, Juan L. Palma, Alejandro Pereira, Juan Escrig, and Samuel E. Baltazar. Mechanical performance of lightweight polycrystalline ni nanotubes. *Computational Materials Science*, 168:81 – 86, 2019.

[178] Hime Aguiar e Oliveira Junior. *Evolutionary Global Optimization, Manifolds and Applications*. Springer International Publishing, 2016.

[179] Ian Goodfellow, Yoshua Bengio, and Aaron Courville. *Deep Learning*. The MIT Press, 2017.

[180] Richard Lesar. *Computational Material Science*. Cambridge University Press, 2013.

[181] Richard M. Martin. *Electronic Structure Basic Theory and Prectical Methods*. Cambridge University Press, 2008.

[182] Robert G. Parr and Weitao Yang. *Density-Functional Theory of Atoms and Molecules*. Oxford University Press, 1989.

[183] Eberhard Engel and Reiner M. Dreizler. *Density Functional Theory*. Springer Berlin Heidelberg, 2011.

[184] Wolfram Koch and Max C. Holthausen. *A Chemist's Guide to Density Functional Theory*. WILEY-VCH, 2001.